# 12

# Sparticle production at colliders

The interaction Lagrangian for the physical particles of the MSSM presented in Chapter 8 can be used to compute the $S$-matrix elements for any physical process, and production cross sections and decay rates can then be obtained. In this chapter, we focus on the evaluation of tree-level superparticle production cross sections in high energy collisions, and present sparticle production rates at currently operating colliders, as well as at colliding beam facilities under construction, or those being considered for construction in the future. We first examine production reactions at hadron colliders such as the Fermilab Tevatron $p\bar{p}$ collider, which is currently operating at a center of mass (CM) energy $\sqrt{s} \simeq 2$ TeV. Negative results of SUSY searches at the Tevatron have been interpreted by the CDF and DØ collaborations as a lower limit $m_{\tilde{g}} \geq 195$ GeV ($m_{\tilde{g}} \geq 260$–$300$ GeV if squarks are degenerate and have a mass equal to $m_{\tilde{g}}$) on the gluino mass. We also show example cross sections for the CERN Large Hadron Collider (LHC), a $pp$ collider, which is scheduled to operate at a CM energy around 14 TeV. The CERN LHC will have sufficient energy to either establish or rule out many models of weak scale supersymmetry. The evaluation of sparticle production rates by hadronic collisions is complicated by the fact that hadrons are not elementary, but composed of quarks and gluons.

In the second section of this chapter, we discuss sparticle production reactions at $e^+e^-$ colliders. Since electrons, unlike protons, are elementary particles, the production processes are much simpler. Searches for supersymmetric matter at the CERN LEP2 $e^+e^-$ collider, which concluded operation in November 2000, have provided significant lower limits on several sparticle masses. The clean environment of $e^+e^-$ scattering events, together with the well-defined energy of the initial state, make these machines ideal for precision measurements of sparticle properties. Designs for linear $e^+e^-$ colliders operating at $\sqrt{s} \simeq 0.5$–$1.5$ TeV and beyond usually include the possibility of longitudinal electron beam polarization and possibly even positron beam polarization. Beam polarization can be a valuable tool, both for eliminating SM backgrounds, as well as for separating signals from different



https://doi.org/10.1017/9781009289801.013 Published online by Cambridge University Press

SUSY reactions. We will, therefore, consider sparticle production from polarized initial beams: results for unpolarized (or partially polarized) beams can be obtained by suitable averaging over polarization.

Leading order formulae for cross sections for sparticle pair production are collected in Appendix A.

## 12.1 Sparticle production at hadron colliders

Since superpartners are assumed to be heavy, sparticle pair production is a high $Q^2$ process, and at hadron colliders occurs predominantly via collisions between the constituents of hadrons: the quarks, antiquarks, and gluons. Production cross sections are calculated within the framework of the parton model.[1] Suppose parton $a$ is a constituent of hadron $A$, and parton $b$ is a constituent of hadron $B$. Parton $a$ carries fractional longitudinal momentum $x_a$ of hadron $A$, and parton $b$ carries fractional longitudinal momentum $x_b$ of hadron $B$. We let $f_{a/A}(x_a, Q^2)$ denote the probability density of finding parton $a$ with fractional momentum $x_a$ in hadron $A$, where $Q^2$ is the squared four-momentum transfer of the underlying elementary process. Its magnitude is the typical energy scale of this reaction. $f_{a/A}(x_a, Q^2)$ is the parton distribution function (PDF). For a hadronic reaction,

$$A + B \to c + d + X,$$

where $c$ and $d$ are superpartners and $X$ represents assorted hadronic debris, we have an associated subprocess reaction

$$a + b \to c + d,$$

whose cross section can be computed using the Lagrangian for the MSSM. To obtain the final cross section, we must convolute the appropriate subprocess production cross section $\mathrm{d}\hat{\sigma}$ with the parton distribution functions:

$$\mathrm{d}\sigma(AB \to cdX) = \sum_{a,b} \int_0^1 \mathrm{d}x_a \int_0^1 \mathrm{d}x_b f_{a/A}(x_a, Q^2)\, f_{b/B}(x_b, Q^2)\, \mathrm{d}\hat{\sigma}(ab \to cd), \tag{12.1}$$

where the sum extends over all initial partons $a, b$ whose collisions produce the final state $c + d$.

Notice that the longitudinal momentum $\mathbf{p}_a + \mathbf{p}_b$ of the initial state is not known. It is for this reason that complete kinematic reconstruction is usually not possible at hadron colliders. The initial partons, however, have negligible transverse

[1] See, e.g., V. Barger and R. J. N. Phillips, *Collider Physics*, Addison-Wesley (1987).

https://doi.org/10.1017/9781009289801.013 Published online by Cambridge University Press

momentum. Constraints from transverse momentum balance, therefore, play a central role in hadron collider physics.

Once the interactions of sparticles are known, the computation of the hard scattering cross section for any sparticle production process is straightforward. One way is to develop the Feynman rules for the MSSM and use these to obtain the production amplitudes and then the cross section.[2] The presence of Majorana neutralinos is an additional complication that leads to somewhat unusual Feynman rules. Instead of following this route, we will describe a procedure for evaluating the invariant matrix element starting from the interaction Lagrangian. In effect, this procedure involves doing exactly what one would do to derive the Feynman rules, and so is not new. We find it convenient to use because all particles are treated uniformly, the relative signs between various amplitudes are automatically obtained, and no new rules have to be committed to memory.

The invariant amplitude $\mathcal{M}$ that enters the computation of the cross section for the process $i \to f$, where $i$ and $f$ denote the initial and final states, respectively, arises from the non-trivial part of the $S$-matrix element

$$\langle f|S|i\rangle = \langle f|T\left(\exp[-\mathrm{i}\int \mathrm{d}^4x\mathcal{H}_{\mathrm{int}}]\right)|i\rangle, \tag{12.2a}$$

where

$$S = 1 + \mathrm{i}(2\pi)^4\delta^4(P_f - P_i)\mathcal{M}. \tag{12.2b}$$

We assume that the reader is familiar with the evaluation of $\mathcal{M}$ using covariant perturbation theory and, in particular, with how various numerical factors coming from different ways of Wick contracting to obtain the same Feynman diagram usually cancel (or sometimes give the so-called combinatorial factor). Once the matrix element $\mathcal{M}$ has been computed, the cross section for the hard scattering process can be readily obtained using,

$$\mathrm{d}\hat{\sigma} = \frac{1}{2\hat{s}}\frac{1}{(2\pi)^2}\int \frac{\mathrm{d}^3p_c}{2E_c}\frac{\mathrm{d}^3p_d}{2E_d}\delta^4(p_a + p_b - p_c - p_d)\cdot F_{\mathrm{color}}F_{\mathrm{spin}}\sum|\mathcal{M}|^2, \tag{12.2c}$$

where $F_{\mathrm{color}}$ and $F_{\mathrm{spin}}$ are factors arising from averaging over the colors and spins in the initial state (assuming it to be unpolarized) and the sum extends over the colors and spins of the initial and final states.

[2] See, e.g., M. E. Peskin and D. V. Schroeder, *Introduction to Quantum Field Theory*, Chapter 4, Perseus Press (1995).

https://doi.org/10.1017/9781009289801.013 Published online by Cambridge University Press

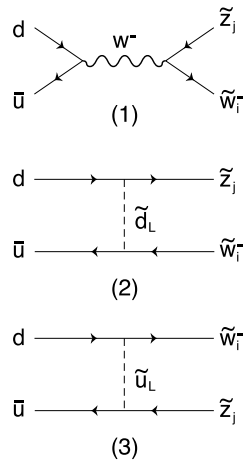


Figure 12.1 Feynman diagrams for chargino–neutralino pair production from quark–antiquark annihilation at hadron colliders.

### 12.1.1 Chargino–neutralino production

*Cross section for $d\bar{u} \to \widetilde{W}_i^- \widetilde{Z}_j$: a worked example*

As an illustration of the method we will work out the cross section for chargino–neutralino production which dominantly occurs by annihilation of quarks and antiquarks at hadron colliders: $d\bar{u} \to \widetilde{W}_i^- \widetilde{Z}_j$. Subdominant contributions from other flavors can be analogously included. In the next chapter, we will see that the subsequent decays of the chargino and the neutralino can lead to a final state with three hard (high $p_T$), isolated leptons ($e$'s or $\mu$'s) plus large missing transverse momentum carried off by the LSPs. This may be one of the best discovery modes for gravity-mediated SUSY breaking models at the Fermilab Tevatron.

The subprocess $d\bar{u} \to \widetilde{W}_i^- \widetilde{Z}_j$ takes place at second order in the perturbation expansion via the three Feynman diagrams listed in Fig. 12.1. The relevant vertices can be obtained from the interaction terms,

$$\mathcal{L}_{W\bar{u}d} = -\frac{g}{\sqrt{2}}\bar{u}\gamma_\mu \frac{1-\gamma_5}{2} d\, W^{+\mu} + \quad \text{h.c.}$$

$$\mathcal{L}_{W\widetilde{W}_i\widetilde{Z}_j} = -g(-\mathrm{i})^{\theta_j}\overline{\widetilde{W}}_i[X_i^j + Y_i^j\gamma_5]\gamma_\mu \widetilde{Z}_j W^{-\mu} + \quad \text{h.c.}$$

$$\mathcal{L}_{q\tilde{q}\widetilde{W}_i} = \mathrm{i}A^d_{\widetilde{W}_i}\tilde{u}_{\mathrm{L}}^\dagger \overline{\widetilde{W}}_i \frac{1-\gamma_5}{2} d + \mathrm{i}A^u_{\widetilde{W}_i}\tilde{d}_{\mathrm{L}}^\dagger \overline{\widetilde{W}_i^c}\frac{1-\gamma_5}{2} u + \quad \text{h.c.}$$

and

$$\mathcal{L}_{q\tilde{q}\widetilde{Z}_j} = \mathrm{i}A^q_{\widetilde{Z}_j}\tilde{q}_{\mathrm{L}}^\dagger \overline{\widetilde{Z}}_j \frac{1-\gamma_5}{2} q + \quad \text{h.c.},$$

listed in Chapter 8.

https://doi.org/10.1017/9781009289801.013 Published online by Cambridge University Press

The amplitude $\mathcal{M}_1$ corresponding to the first of the diagrams in Fig. 12.1 obviously depends on the matrix element,

$$\langle \widetilde{W}_i \widetilde{Z}_j | T \left[ \left( -g(-\mathrm{i})^{\theta_j} \overline{\widetilde{W}}_i [X_i^j + Y_i^j \gamma_5] \gamma_\mu \widetilde{Z}_j W^{-\mu}(x) \right) \right.$$
$$\left. \times \left( -\frac{g}{\sqrt{2}} \bar{u} \gamma_\nu \frac{1-\gamma_5}{2} d W^{+\nu}(y) \right) \right] | d\bar{u} \rangle,$$

where the two interactions occur at different spacetime points $x$ and $y$ whose coordinates are ultimately integrated over. We then proceed as follows:

1. The particles in the initial (final) state are then "reduced" in any chosen order (which we take to be $d$, $\bar{u}$, $\widetilde{Z}_j$, $\widetilde{W}_i$) using the annihilation (creation) pieces of the corresponding fermion operators. To carry out this reduction, the corresponding field operator must be moved next to the state in question. Since fermion fields anticommute with other fermion fields, this process can lead to minus signs. In the present case, the reduction of the quarks in the prescribed order does not lead to any sign, but to reduce the neutralino in the final state one has to anticommute the $\widetilde{Z}_j(x)$ past $\overline{\widetilde{W}}_i(x)$, giving an additional minus sign for this amplitude. The reduction of the Dirac quarks [antiquarks] in the initial state and the chargino in the final state, as usual, leaves wave function factors $u(p_d)\exp(-\mathrm{i}p_d \cdot y)$ $[\bar{v}(p_{\bar{u}})\exp(-\mathrm{i}p_{\bar{u}} \cdot y)]$, and $\bar{u}(p_{\widetilde{W}_j})\exp(\mathrm{i}p_{\widetilde{W}_j} \cdot x)$. Notice that because the neutralino is Majorana, it can be reduced by the operator $\widetilde{Z}_j(x)$ (as opposed to its Dirac conjugate) even though it is in the final state. In other words, the neutralino is treated as an anti-particle, and the associated wave function factor is, $v(p_{\widetilde{Z}_j})exp(\mathrm{i}p_{\widetilde{Z}_j} \cdot x)$. This is also the reason for the reversed direction of the arrow (which denotes the flow of fermion number) on the neutralino line in diagram (1) of Fig. 12.1.
2. Once the external particles are all reduced, aside from $c$-number wave function and coupling constant factors, we are left with

$$\langle 0 | T(W^{-\mu}(x) W^{+\nu}(y)) | 0 \rangle$$

which is of course the propagator for the $W$-boson between the spacetime points $x$ and $y$. For the final step, it is convenient to write this propagator (in the unitary gauge) in terms of its momentum space expansion with the four-momentum variable $q_W$ as

$$\langle 0 | T \left( W^{-\mu}(x) W^{+\nu}(y) \right) | 0 \rangle = \mathrm{i} \int \frac{\mathrm{d}^4 q_W}{(2\pi)^4} \frac{-g^{\mu\nu} + \frac{q_W^\mu q_W^\nu}{M_W^2}}{q_W^2 - M_W^2 + \mathrm{i} M_W \Gamma_W} \mathrm{e}^{-\mathrm{i} q_W \cdot (x-y)}.$$

3. Finally, integration over $x$ and $y$ leads to four-momentum conservation at each vertex (so that the propagator momentum $q_W = p_d + p_{\bar{u}}$), leaving us with an

https://doi.org/10.1017/9781009289801.013 Published online by Cambridge University Press

overall four-momentum conserving $\delta$ function as in the last term of (12.2b). Neglecting quark masses, the $q_W^\mu q_W^\nu$ term in the propagator cannot contribute because

$$\not{p}_d u(p_d) = \bar{v}(p_{\bar{u}})\not{p}_{\bar{u}} = 0,$$

by the Dirac equation. All factors of $(2\pi)$ cancel and there is no combinatorial factor. We are left with[3]

$$\mathcal{M}_1 = \frac{g^2}{\sqrt{2}}(-\mathrm{i})^{\theta_j} D_W(\hat{s})\bar{u}(\widetilde{W}_i)[X_i^j + Y_i^j\gamma_5]\gamma^\mu v(\widetilde{Z}_j)\,\bar{v}(\bar{u})\gamma_\mu\frac{1-\gamma_5}{2}u(d). \quad (12.3a)$$

Here particle labels denote the corresponding four-momenta, $\hat{s} = (d+\bar{u})^2$, and $D_W(\hat{s}) = (\hat{s} - M_W^2 + \mathrm{i}M_W\Gamma_W)^{-1}$.

The amplitude for the $\tilde{d}_\mathrm{L}$ exchange diagram (2) in Fig. 12.1 depends on the matrix element,

$$\langle \widetilde{W}_i\widetilde{Z}_j|T\left[\left(\mathrm{i}A^d_{\widetilde{Z}_j}\tilde{d}_\mathrm{L}^\dagger\overline{\widetilde{Z}}_j\frac{1-\gamma_5}{2}d\right)\left(-\mathrm{i}A^{u*}_{\widetilde{W}_i}\tilde{d}_\mathrm{L}\bar{u}\frac{1+\gamma_5}{2}\widetilde{W}_i^c\right)\right]|d\bar{u}\rangle.$$

The reduction of the $d$ and $\bar{u}$ quarks in the initial state gives the usual Dirac wave functions for these. This time, the neutralino is reduced by the operator $\overline{\widetilde{Z}}_j$ (so that it is treated as a particle rather than as an antiparticle as in the evaluation of $\mathcal{M}_1$). Finally, the chargino is reduced by the creation part of the $\widetilde{W}_i^c$ operator (which destroys a positive chargino or creates a negative chargino), and by the expansion analogous to (3.33) we obtain the wave function $v(\widetilde{W}_i)\exp(\mathrm{i}\widetilde{W}_i\cdot x)$ for the chargino. Notice that the directions of the arrows on the chargino and neutralino lines in diagram (2) of Fig. 12.1 are in accord with this assignment. The scalar field operators contract together to form the $\tilde{d}_\mathrm{L}$ propagator, and the corresponding amplitude can be written as,

$$\mathcal{M}_2 = -A^d_{\widetilde{Z}_j}A^{u*}_{\widetilde{W}_i}\bar{u}(\widetilde{Z}_j)\frac{1-\gamma_5}{2}u(d)\frac{1}{(\widetilde{W}_i-\bar{u})^2 - m^2_{\tilde{d}_\mathrm{L}}}\bar{v}(\bar{u})\frac{1+\gamma_5}{2}v(\widetilde{W}_i), \quad (12.3b)$$

where, once again, there is an additional minus sign from anticommuting fermion field operators. We will leave it to the reader to work out that the amplitude for the

[3] In writing (12.3a) we have left out a factor $(\mathrm{i})^3$ where two powers of i come from the fact that we are doing second order perturbation theory, and the third power of i comes from the propagator. Since all three diagrams come from second order perturbation theory, and each of these contains one propagator, this amounts to leaving out an irrelevant phase in the overall amplitude from the way it is conventionally written. Moreover, from (12.2b) we see that what we have evaluated is really $\mathrm{i}\mathcal{M}_1$ rather than $\mathcal{M}_1$; again, this only changes the overall phase. We will omit these irrelevant phase factors in the rest of this book. We warn the reader that one should be careful in doing so. In calculations where the amplitude comes from contributions with different numbers of propagators, or from different orders of expansion (although with the same powers of couplings, of course) of the time evolution operator, these phases must be retained.

https://doi.org/10.1017/9781009289801.013 Published online by Cambridge University Press

$\tilde{u}_{\rm L}$ exchange diagram (3) that depends on the matrix element

$$\langle \widetilde{W}_i \widetilde{Z}_j | T \left[ \left( -\mathrm{i} A^{u*}_{\widetilde{Z}_j} \bar{u} \frac{1+\gamma_5}{2} \widetilde{Z}_j \tilde{u}_{\rm L} \right) \left( \mathrm{i} A^{d}_{\widetilde{W}_i} \tilde{u}^{\dagger}_{\rm L} \overline{\widetilde{W}_i} \frac{1-\gamma_5}{2} d \right) \right] | d \bar{u} \rangle,$$

takes the form.

$$\mathcal{M}_3 = A^{d}_{\widetilde{W}_i} A^{u*}_{\widetilde{Z}_j} \bar{v}(\bar{u}) \frac{1+\gamma_5}{2} v(\widetilde{Z}_j) \frac{1}{(\widetilde{Z}_j - \bar{u})^2 - m^2_{\tilde{u}_{\rm L}}} \bar{u}(\widetilde{W}_i) \frac{1-\gamma_5}{2} u(d). \quad (12.3c)$$

Note that constructing the amplitudes in this fashion allows us to keep track of the relative signs between them.

The amplitudes $\mathcal{M}_1$, $\mathcal{M}_2$, and $\mathcal{M}_3$ can now be squared and summed over initial and final spin states using standard trace techniques. We find,

$$\begin{aligned} \sum_{\text{spins}} |\mathcal{M}_1|^2 = 8 g^4 |D_W(\hat{s})|^2 \Big\{ & [X_i^{j2} + Y_i^{j2}] (\widetilde{Z}_j \cdot d \widetilde{W}_i \cdot \bar{u} + \widetilde{Z}_j \cdot \bar{u} \widetilde{W}_i \cdot d) \\ & + 2 (X_i^j Y_i^j) (\widetilde{Z}_j \cdot d \widetilde{W}_i \cdot \bar{u} - \widetilde{Z}_j \cdot \bar{u} \widetilde{W}_i \cdot d) \\ & + [X_i^{j2} - Y_i^{j2}] m_{\widetilde{W}_i} m_{\widetilde{Z}_j} d \cdot \bar{u} \Big\}, \end{aligned} \quad (12.4a)$$

$$\sum_{\text{spins}} |\mathcal{M}_2|^2 = \frac{4 |A^{u}_{\widetilde{W}_i}|^2 |A^{d}_{\widetilde{Z}_j}|^2}{[(\widetilde{W}_i - \bar{u})^2 - m^2_{\tilde{d}_{\rm L}}]^2} \, d \cdot \widetilde{Z}_j \widetilde{W}_i \cdot \bar{u} \quad (12.4b)$$

and

$$\sum_{\text{spins}} |\mathcal{M}_3|^2 = \frac{4 |A^{d}_{\widetilde{W}_i}|^2 |A^{u}_{\widetilde{Z}_j}|^2}{[(\widetilde{Z}_j - \bar{u})^2 - m^2_{\tilde{u}_{\rm L}}]^2} \, \bar{u} \cdot \widetilde{Z}_j \widetilde{W}_i \cdot d. \quad (12.4c)$$

Next, we turn to the interference terms between these amplitudes. Here we will often find a "mismatch" of spinors. For instance, in computing $\sum_{\text{spins}} (\mathcal{M}_1 \mathcal{M}_2^{\dagger})$, we find

$$\begin{aligned} \sum_{\text{spins}} \mathcal{M}_1 \mathcal{M}_2^{\dagger} = -(-\mathrm{i})^{\theta_j} \frac{g^2}{\sqrt{2}} D_W(\hat{s}) \frac{1}{(\widetilde{W}_i - \bar{u})^2 - m^2_{\tilde{d}_{\rm L}}} A^{d*}_{\widetilde{Z}_j} A^{u}_{\widetilde{W}_i} \\ \times \bar{u}(\widetilde{W}_i) (X_i^j + Y_i^j \gamma_5) \gamma^{\mu} v(\widetilde{Z}_j) \cdot \bar{v}(\bar{u}) \gamma_{\mu} \frac{1-\gamma_5}{2} u(d) \\ \times \bar{u}(d) \frac{1+\gamma_5}{2} u(\widetilde{Z}_j) \cdot \bar{v}(\widetilde{W}_i) \frac{1-\gamma_5}{2} v(\bar{u}), \end{aligned}$$

so that the chargino and neutralino spinors are not in the proper format for us to evaluate the spin sums using as usual

$$\sum_{\text{spins}} u(p) \bar{u}(p) = \not{p} + m,$$

https://doi.org/10.1017/9781009289801.013 Published online by Cambridge University Press

etc. In order to do the spin sums using the spinor completeness relations, we may use the relations $u = C\bar{v}^T$ and $v = C\bar{u}^T$ to write,

$$\begin{aligned}\bar{u}(\widetilde{W}_i)(X_i^j + Y_i^j\gamma_5)\gamma^\mu v(\widetilde{Z}_j) &= v^T(\widetilde{W}_i)C(X_i^j + Y_i^j\gamma_5)\gamma^\mu C\bar{u}^T(\widetilde{Z}_j)\\ &= v^T(\widetilde{W}_i)(X_i^j + Y_i^j\gamma_5)^T\gamma^{\mu T}\bar{u}^T(\widetilde{Z}_j)\\ &= \bar{u}(\widetilde{Z}_j)\gamma^\mu(X_i^j + Y_i^j\gamma_5)v(\widetilde{W}_i).\end{aligned}$$

Now we may apply the spinor completeness relations and follow the usual trace techniques to obtain,

$$\begin{aligned}\sum_{\text{spins}}(\mathcal{M}_1\mathcal{M}_2^* + \quad \text{c.c.}) = &\frac{-\sqrt{2}g^2\text{Re}[A^{d*}_{\widetilde{Z}_j}A^{u}_{\widetilde{W}_i}(-\text{i})^{\theta_j}](\hat{s} - M_W^2)|D_W(\hat{s})|^2}{(\widetilde{W}_i - \bar{u})^2 - m^2_{\tilde{d}_\text{L}}}\\ &\times\left\{8(X_i^j + Y_i^j)\widetilde{Z}_j\cdot d\bar{u}\cdot\widetilde{W}_i + 4(X_i^j - Y_i^j)m_{\widetilde{W}_i}m_{\widetilde{Z}_j}d\cdot\bar{u}\right\}.\end{aligned} \tag{12.4d}$$

Similarly, we find that

$$\begin{aligned}\sum_{\text{spins}}(\mathcal{M}_1\mathcal{M}_3^* + \quad \text{c.c.}) = &\frac{\sqrt{2}g^2\text{Re}[A^{d*}_{\widetilde{W}_i}A^{u}_{\widetilde{Z}_j}(-\text{i})^{\theta_j}](\hat{s} - M_W^2)|D_W(\hat{s})|^2}{(\widetilde{Z}_j - \bar{u})^2 - m^2_{\tilde{u}_\text{L}}}\\ &\times\left\{8(X_i^j - Y_i^j)\widetilde{Z}_j\cdot\bar{u}d\cdot\widetilde{W}_i + 4(X_i^j + Y_i^j)m_{\widetilde{W}_i}m_{\widetilde{Z}_j}d\cdot\bar{u}\right\},\end{aligned} \tag{12.4e}$$

and

$$\sum_{\text{spins}}(\mathcal{M}_2\mathcal{M}_3^* + \quad \text{c.c.}) = -\frac{4\text{Re}[A^{d}_{\widetilde{Z}_j}A^{u*}_{\widetilde{W}_i}A^{d*}_{\widetilde{W}_i}A^{u}_{\widetilde{Z}_j}]m_{\widetilde{W}_i}m_{\widetilde{Z}_j}d\cdot\bar{u}}{[(\widetilde{W}_i - \bar{u})^2 - m^2_{\tilde{d}_\text{L}}][(\widetilde{Z}_j - \bar{u})^2 - m^2_{\tilde{u}_\text{L}}]}. \tag{12.4f}$$

The hard subprocess cross section is obtained using,

$$\text{d}\hat{\sigma} = \frac{1}{2\hat{s}}\frac{1}{(2\pi)^2}\int\frac{\text{d}^3p_{\widetilde{W}_i}}{2E_{\widetilde{W}_i}}\frac{\text{d}^3p_{\widetilde{Z}_j}}{2E_{\widetilde{Z}_j}}\delta^4(\bar{u} + d - \widetilde{W}_i - \widetilde{Z}_j)\cdot\frac{1}{3}\frac{1}{4}\sum_{\text{spins}}|\mathcal{M}|^2, \tag{12.5a}$$

or

$$\frac{\text{d}\hat{\sigma}}{\text{d}\cos\theta} = \frac{p_{\widetilde{W}_i}}{16\pi\hat{s}^{3/2}}\frac{1}{12}\sum_{\text{spins}}|\mathcal{M}|^2, \tag{12.5b}$$

where

$$p_{\widetilde{W}_i} = p_{\widetilde{Z}_j} = \lambda^{1/2}(\hat{s}, m^2_{\widetilde{W}_i}, m^2_{\widetilde{Z}_j})/2\sqrt{\hat{s}}, \tag{12.6a}$$

https://doi.org/10.1017/9781009289801.013 Published online by Cambridge University Press

with

$$\lambda(x, y, z) = x^2 + y^2 + z^2 - 2xy - 2xz - 2yz. \tag{12.6b}$$

The factor $1/3$ $(1/4)$ in (12.5a) comes from averaging over color (spin) in the initial state. A sum over colors in the initial and (when applicable) final states is implied. Since the squared matrix element given by the sum of (12.4a)–(12.4f) is Lorentz invariant, we can evaluate it in any frame. It is convenient to evaluate it in the CM frame of the colliding partons. There is no loss of generality if we choose their directions to be along the $\pm z$-axis, and take the chargino and neutralino to lie in the $xz$ plane. Their four vectors can thus be written as:

$$d = \frac{\sqrt{\hat{s}}}{2}(1,\ 0,\ 0,\ 1), \tag{12.7a}$$

$$\bar{u} = \frac{\sqrt{\hat{s}}}{2}(1,\ 0,\ 0,\ -1), \tag{12.7b}$$

$$\widetilde{W}_i = (E_{\widetilde{W}_i},\ p_{\widetilde{W}_i}\sin\theta,\ 0,\ p_{\widetilde{W}_i}\cos\theta), \tag{12.7c}$$

$$\widetilde{Z}_j = (E_{\widetilde{Z}_j},\ -p_{\widetilde{Z}_j}\sin\theta,\ 0,\ -p_{\widetilde{Z}_j}\cos\theta). \tag{12.7d}$$

We can now evaluate all the scalar products that appear in the squared matrix element in terms of the scattering angle $\theta$ in the parton CM frame, and obtain our result for the differential scattering cross section for the hard process $\mathrm{d}\bar{u} \to \widetilde{W}_i \widetilde{Z}_j$ in terms of $z = \cos\theta$ as,

$$\frac{\mathrm{d}\hat{\sigma}}{\mathrm{d}z}(d\bar{u} \to \widetilde{W}_i \widetilde{Z}_j) = \frac{p_{\widetilde{W}_i}}{16\pi\hat{s}^{3/2}}\frac{1}{12}\left(M_1 + M_2 + M_3 + M_{12} + M_{13} + M_{23}\right), \tag{12.8}$$

where

$$M_1 = g^4|D_W(\hat{s})|^2\left\{(X_i^{j2} + Y_i^{j2})\left[\hat{s}^2 - (m^2_{\widetilde{W}_i} - m^2_{\widetilde{Z}_j})^2 + 4\hat{s}\,p^2_{\widetilde{W}_i}z^2\right]\right.$$
$$\left. + 8X_i^j Y_i^j \hat{s}^{3/2}pz + 4(X_i^{j2} - Y_i^{j2})\hat{s}m_{\widetilde{W}_i}m_{\widetilde{Z}_j}\right\} \tag{12.9a}$$

$$M_2 = \frac{1}{4}|A^d_{\widetilde{Z}_j}|^2|A^u_{\widetilde{W}_i}|^2\ G(m_{\widetilde{Z}_j}, m_{\widetilde{W}_i}, m_{\tilde{d}_\mathrm{L}}, -z) \tag{12.9b}$$

$$M_3 = \frac{1}{4}|A^d_{\widetilde{W}_i}|^2|A^u_{\widetilde{Z}_j}|^2\ G(m_{\widetilde{W}_i}, m_{\widetilde{Z}_j}, m_{\tilde{u}_\mathrm{L}}, z) \tag{12.9c}$$

$$M_{12} = \frac{\frac{g^2}{\sqrt{2}}\mathrm{Re}[(-\mathrm{i})^{\theta_j}A^u_{\widetilde{W}_i}A^{d*}_{\widetilde{Z}_j}](\hat{s} - M_W^2)|D_W(\hat{s})|^2}{[\frac{1}{2}(\hat{s} - m^2_{\widetilde{Z}_j} - m^2_{\widetilde{W}_i}) + \sqrt{\hat{s}}pz + m^2_{\tilde{d}_\mathrm{L}}]}\left\{(X_i^j + Y_i^j)\right.$$
$$\left.[\hat{s}^2 - (m^2_{\widetilde{W}_i} - m^2_{\widetilde{Z}_j})^2 + 4\hat{s}^{3/2}pz + 4\hat{s}\,p^2z^2] + 4(X_i^j - Y_i^j)\hat{s}m_{\widetilde{W}_i}m_{\widetilde{Z}_j}\right\} \tag{12.9d}$$

https://doi.org/10.1017/9781009289801.013 Published online by Cambridge University Press

$$M_{13} = \frac{-\frac{g^2}{\sqrt{2}}\mathrm{Re}[(-\mathrm{i})^{\theta_j} A^u_{\widetilde{Z}_j} A^{d*}_{\widetilde{W}_i}](\hat{s} - M_W^2)|D_W(\hat{s})|^2}{[\frac{1}{2}(\hat{s} - m^2_{\widetilde{Z}_j} - m^2_{\widetilde{W}_i}) - \sqrt{\hat{s}}pz + m^2_{\tilde{u}_\mathrm{L}}]} \Big\{(X_i^j - Y_i^j)$$
$$[\hat{s}^2 - (m^2_{\widetilde{W}_i} - m^2_{\widetilde{Z}_j})^2 - 4\hat{s}^{3/2}pz + 4\hat{s}p^2z^2] + 4(X_i^j + Y_i^j)\hat{s}m_{\widetilde{W}_i}m_{\widetilde{Z}_j}\Big\} \quad (12.9e)$$

$$M_{23} = \frac{-2\mathrm{Re}[A^d_{\widetilde{Z}_j} A^{u*}_{\widetilde{W}_i} A^{d*}_{\widetilde{W}_i} A^u_{\widetilde{Z}_j}]\hat{s}m_{\widetilde{W}_i}m_{\widetilde{Z}_j}}{[\frac{1}{2}(\hat{s} - m^2_{\widetilde{Z}_j} - m^2_{\widetilde{W}_i}) - \sqrt{\hat{s}}pz + m^2_{\tilde{u}_\mathrm{L}}][\frac{1}{2}(\hat{s} - m^2_{\widetilde{Z}_j} - m^2_{\widetilde{W}_i}) + \sqrt{\hat{s}}pz + m^2_{\tilde{d}_\mathrm{L}}]}, \quad (12.9f)$$

where

$$G(m_1, m_2, M, z) = \frac{\hat{s}^2 - (m_1^2 - m_2^2)^2 - 4\hat{s}^{3/2}pz + 4\hat{s}p^2z^2}{[\frac{1}{2}(\hat{s} - m_1^2 - m_2^2) - \sqrt{\hat{s}}pz + M^2]^2}. \quad (12.10)$$

It is not difficult to integrate the subprocess cross section over scattering angles to obtain the total cross section. For the purposes of event generation at hadron colliders, discussed in Chapter 14, this is not especially useful and, although expressions for these total cross sections are available, we do not reproduce these here. In any event, to obtain the total cross section at a hadron collider, we must convolute this subprocess cross section with appropriate PDFs. This is done numerically. Throughout this book, we use CTEQ5L PDFs.[4] Here, we take the renormalization and factorization scales equal, and equal to $Q^2 = \hat{s}$. As an example, various chargino–neutralino production cross sections are shown in Fig. 12.2 versus $m_{\tilde{g}}$ for the CERN LHC $pp$ collider. We have assumed that all flavors of $\tilde{q}_\mathrm{L}$ that enter via the $t$-channel propagators have a common mass.[5] In this figure, we have taken the superpotential parameter $\mu = m_{\tilde{g}} = m_{\tilde{q}}$ and $\tan\beta = 5$. We also assume the gaugino mass unification condition that relates weak scale gaugino mass parameters according to

$$\frac{M_1}{\alpha_1} = \frac{M_2}{\alpha_2} = \frac{M_3}{\alpha_3},$$

where $\alpha_i = g_i^2/4\pi$ for $i = 1, 2, 3$ and $g_1 = \sqrt{5/3}g'$, $g_2 = g$, and $g_3 = g_s$. The region to the left of the vertical line is excluded by experiments at LEP2, since they require $m_{\widetilde{W}_1} \gtrsim 100$ GeV.

By far the dominant cross section in this class of models occurs for $\widetilde{W}_1\widetilde{Z}_2$ production. Gaugino mass unification implies roughly $M_1 : M_2 : M_3 \simeq 1 : 2 : 7$. Since

[4] H. L. Lai *et al.* (CTEQ Collaboration), *Eur. Phys. J.* **C12**, 375 (2000).
[5] For the purpose of illustrating the various cross sections, in this chapter, we will take all 12 flavors of squarks to be degenerate.

https://doi.org/10.1017/9781009289801.013 Published online by Cambridge University Press

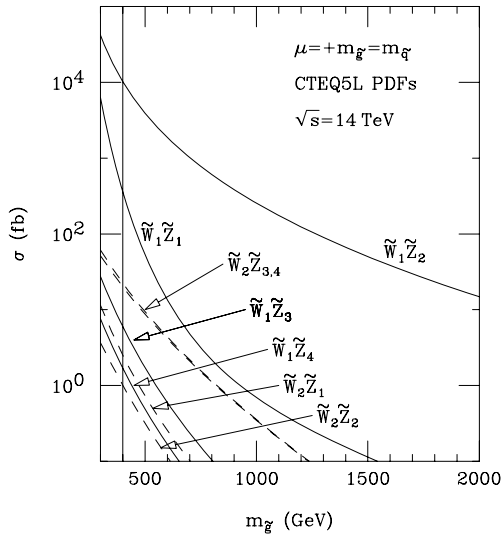


Figure 12.2 Cross sections for chargino plus neutralino production at the CERN LHC $pp$ collider for $\tan\beta = 5$, and assuming gaugino mass unification at $M_{\rm GUT}$. The vertical line corresponds to $m_{\widetilde{W}_1} = 100$ GeV.

$\mu \gg M_2,\ M_1$, the $\widetilde{Z}_1$ will be mainly bino-like (i.e. $\widetilde{Z}_1 \simeq \lambda_0$), while $\widetilde{Z}_2$ and $\widetilde{W}_1$ will be wino-like. Electroweak gauge symmetry implies that the $W$ boson cannot couple to the bino, so that $\widetilde{Z}_1$ couples to $W$ only via its small wino and higgsino components. The wino-like $\widetilde{Z}_2$ and $\widetilde{W}_1$, on the other hand, have large $SU(2)_{\rm L}$ gaugino components, and so have large couplings to the $W$ as well as to the quark–squark system. The states $\widetilde{Z}_3$, $\widetilde{Z}_4$, and $\widetilde{W}_2$ are mainly higgsino-like and so have smaller isodoublet (rather than the larger isotriplet) coupling to $W$; this, as well as kinematics, suppresses their production compared to their gaugino-like cousins. This explains why $\widetilde{W}_1\widetilde{Z}_2$ production has the largest cross section in Fig. 12.2. Even for values of $m_{\tilde{g}}$ as high as 2000 GeV, over 1000 $\widetilde{W}_1\widetilde{Z}_2$ events are expected at the CERN LHC, assuming 100 fb$^{-1}$ of integrated luminosity. At the Fermilab Tevatron collider, $\widetilde{W}_1\widetilde{Z}_2$ production could be the dominant SUSY production reaction because production of colored particles is kinematically suppressed in many models. If the branching ratios for the decays $\widetilde{W}_1 \to \ell\bar{\nu}_\ell\widetilde{Z}_1$ and $\widetilde{Z}_2 \to \ell\bar{\ell}\widetilde{Z}_1$ are large enough then, as already noted, isolated trilepton plus missing energy events may provide a distinctive signature for the discovery of SUSY at the Fermilab Tevatron.

### *12.1.2 Chargino pair production*

At leading order, chargino pair production occurs by $d\bar{d}$ annihilation via the diagrams shown in Fig. 12.3; there are corresponding contributions from annihilation

https://doi.org/10.1017/9781009289801.013 Published online by Cambridge University Press

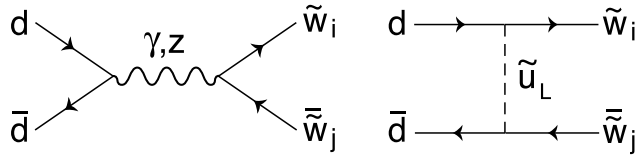


Figure 12.3 Feynman diagrams for leading order chargino pair production via $d\bar{d}$ annihilation at hadron colliders. There are analogous diagrams from the annihilation of other quark flavors.

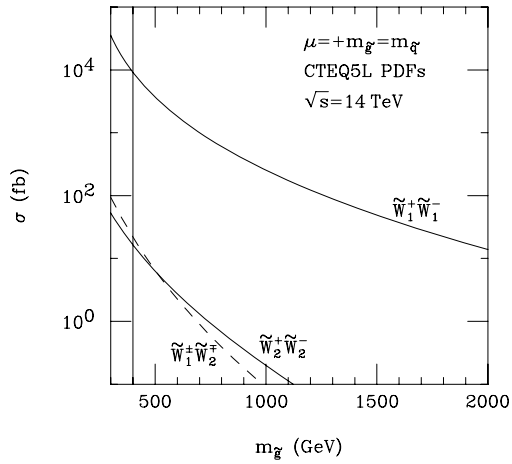


Figure 12.4 Cross sections for chargino pair production at the CERN LHC $pp$ collider for $\tan\beta = 5$, and assuming gaugino mass unification at $M_{\rm GUT}$.

of other quark flavors. The possible final states consist of $\widetilde{W}_1\overline{\widetilde{W}}_1$, $\widetilde{W}_2\overline{\widetilde{W}}_2$, and $\widetilde{W}_1\overline{\widetilde{W}}_2 + \overline{\widetilde{W}}_1\widetilde{W}_2$. The first two of these occur via $\gamma$ or $Z$ exchange in the $s$-channel and $t$-channel squark exchange, while $\widetilde{W}_1\overline{\widetilde{W}}_2 + \overline{\widetilde{W}}_1\widetilde{W}_2$ production occurs only via $Z$ exchange in the $s$-channel and $t$-channel squark exchange. This is because conservation of the electromagnetic current forbids the coupling of the photon to particles of unequal mass. The relevant couplings are listed in Chapter 8, and can be used to construct the production amplitudes as in the previous section. These can be squared using the same techniques described in the last sub-section. The resulting subprocess cross sections are listed in (A.1)–(A.2) of Appendix A. As before, we convolute with CTEQ5L PDFs, and illustrate the total production cross sections for chargino pair production at the LHC in Fig. 12.4. We see that $\widetilde{W}_1\overline{\widetilde{W}}_1$ production is the largest of this set, and is comparable in magnitude to the cross section for $\widetilde{W}_1\widetilde{Z}_2$ pair production shown in Fig. 12.2.

https://doi.org/10.1017/9781009289801.013 Published online by Cambridge University Press

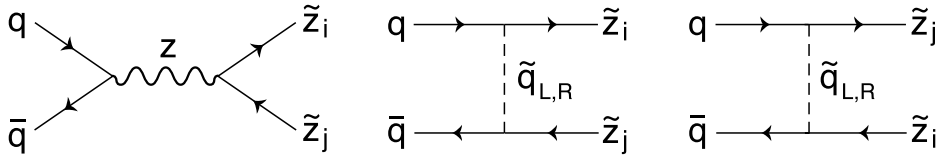


Figure 12.5 Feynman diagrams for leading order neutralino pair production processes at hadron colliders.

### *12.1.3 Neutralino pair production*

Production of neutralino pairs occurs via the diagrams shown in Fig. 12.5. The four $t$-channel amplitudes are straightforward to calculate, but there is a small subtlety in the evaluation of the $s$-channel amplitude represented by the first diagram in the figure coming from the Majorana nature of the neutralino (see the exercise below).

The differential cross section for the ten possible $\widetilde{Z}_i\widetilde{Z}_j$ combinations (corresponding to $i, j = 1$–$4$) is given by (A.3) of Appendix A. When integrating these to obtain the total cross section, we must be careful to distinguish between $i \neq j$ and $i = j$. In the former case, scattering by angle $\theta$ and by angle $\pi - \theta$ correspond to *different* final states since one can distinguish the neutralinos by their mass (or, if there is an accidental degeneracy, by their coupling). Since the total cross section is obtained by summing over all possible final states, we obtain this by integrating the differential cross section over the entire phase space: i.e. over $0 \leq \theta \leq \pi$. However, for $i = j$, all one can say is that there is one neutralino at an angle $\theta$ (with respect to the quark beam) and a second neutralino at an angle $\pi - \theta$, but there is no way to tell, even in principle, which of the two neutralinos is at $\theta$. In other words, *the state with scattering angle $\theta$ is the same state as the one with scattering angle $\pi - \theta$*, and so, to obtain the total cross section we should integrate over just half the phase space (since otherwise we would double count the final states). We can write the total neutralino cross section as,

$$\sigma_{\rm tot}(q\bar{q} \to \widetilde{Z}_i\widetilde{Z}_j) = \Delta_{ij}\int_{-1}^{1}\frac{{\rm d}\sigma}{{\rm d}z}(q\bar{q} \to \widetilde{Z}_i\widetilde{Z}_j){\rm d}z \tag{12.11a}$$

with

$$\Delta_{ij} = 1 - \frac{1}{2}\delta_{ij}. \tag{12.11b}$$

Neutralino pair production rates (particularly for the gaugino-like neutralinos) are more sensitive to model parameters than corresponding rates for $\widetilde{W}_i\widetilde{Z}_j$ and $\widetilde{W}_i^-\widetilde{W}_j^+$ production. This is because they couple to $Z$ only via their small higgsino components (so that the $s$-channel amplitude is suppressed) while the $t$-channel amplitude is obviously sensitive to the squark mass. This is in sharp contrast to $\widetilde{W}_1\widetilde{Z}_2$ production for which we saw that (as long as $|\mu| \gg M_2 \simeq 2M_1$) the

https://doi.org/10.1017/9781009289801.013 Published online by Cambridge University Press

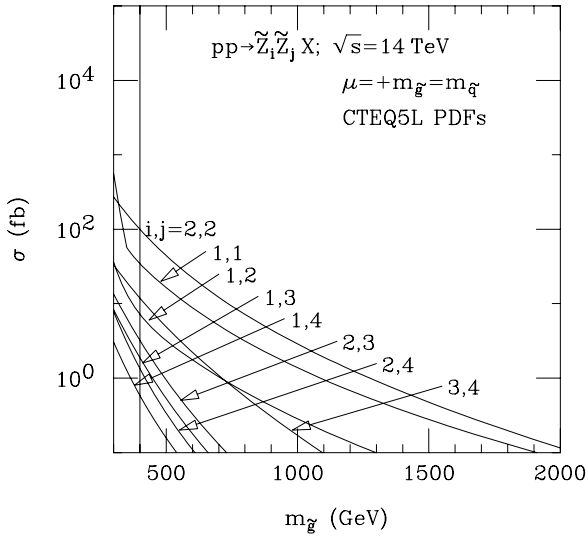


Figure 12.6 Cross sections for neutralino pair production at the CERN LHC $pp$ collider for $\tan\beta = 5$, and assuming gaugino mass unification at $M_{\rm GUT}$.

$W$ amplitude is always large. The $s$-channel contributions are also always sizable for the case of $\widetilde{W}_1^-\widetilde{W}_1^+$ production: the chargino obviously always couples to the photon, and the $Z$ has large weak-isovector couplings to the gaugino-like chargino.

Sample cross sections for the CERN LHC are shown in Fig. 12.6. For the parameters in this figure, the gaugino-like neutralino states, $\widetilde{Z}_2$ and $\widetilde{Z}_1$, are most strongly produced. In models with a $\widetilde{Z}_1$ LSP and $R$-parity conservation, the $\widetilde{Z}_1$ is absolutely stable, and will escape detection at collider detectors. Thus, the $\widetilde{Z}_1\widetilde{Z}_1$ reaction would be invisible, aside from any initial state QCD radiation into instrumented regions of the detector. Many of these reactions occur at low rates and do not lead to distinctive signatures at hadron colliders.

---

**Exercise** *The amplitude for the first diagram in Fig. 12.5 depends on the matrix element*

$$\langle \widetilde{Z}_j\widetilde{Z}_i|e\bar{q}\gamma_\mu(\alpha_q+\beta_q\gamma_5)qZ^\mu\sum_{ab}W_{ab}\overline{\widetilde{Z}}_a\gamma_\nu(\gamma_5)^{\theta_a+\theta_b+1}\widetilde{Z}_bZ^\nu|q\bar{q}\rangle.$$

*The matrix element is non-zero only when either $a = i$ with $b = j$ or $a = j$ with $b = i$. Both these contributions must be included to correctly obtain the amplitude. Evaluate these contributions and, using $W_{ij} = (-1)^{\theta_j-\theta_i}W_{ji}$ together with the charge conjugation properties $u = C\bar{v}^T$ and $v = C\bar{u}^T$ of the solutions to the Dirac equation, show that the two contributions are equal.*

---

https://doi.org/10.1017/9781009289801.013 Published online by Cambridge University Press

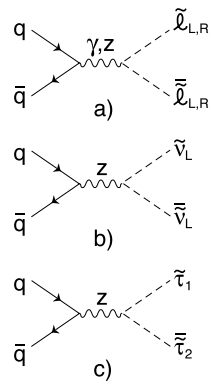


Figure 12.7 Feynman diagrams for leading order slepton pair production at hadron colliders.

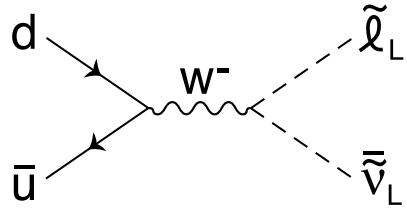


Figure 12.8 Feynman diagram for slepton–sneutrino associated production at hadron colliders.

### *12.1.4 Slepton and sneutrino pair production*

At leading order, charged sleptons and sneutrinos may be produced in pairs via the diagrams in Fig. 12.7, or charged sleptons can be produced in association with their sneutrino partner via the $W$ exchange diagram shown in Fig. 12.8. The former correspond to the supersymmetric analogue of the Drell–Yan process, whereas the latter is the analogue of the classic process via which the $W$ boson was discovered at the CERN $p\bar{p}$ collider. Only like-type (L or R) slepton pairs can be produced for the first two generations of charged sleptons though intrageneration mixing also allows $\tilde{\tau}_1\bar{\tilde{\tau}}_2 + \bar{\tilde{\tau}}_1\tilde{\tau}_2$ production via $Z$ exchange. Since $W$ couples only to left-handed leptons and their superpartners, $\tilde{\ell}_R\tilde{\nu}_L$ production is forbidden. Both $\tilde{\tau}_1$ and $\tilde{\tau}_2$ can be produced in association with $\tilde{\nu}_\tau$; the state with the large admixture of $\tilde{\tau}_L$ ($\tilde{\tau}_2$ in many models) has the bigger coupling to $W$.

The computation of the various amplitudes differs from what we have already seen only because of the derivative coupling of sleptons to gauge bosons. To illustrate how these are handled, we write the amplitude for the associated

https://doi.org/10.1017/9781009289801.013 Published online by Cambridge University Press

slepton–sneutrino production process in Fig. 12.8. We need to evaluate the matrix element,

$$\langle \tilde{\ell}\tilde{\nu}_{\rm L} \left| T\left[\left(-\frac{g}{\sqrt{2}}\bar{u}\gamma^{\mu}\frac{1-\gamma_5}{2}dW_{\mu}^{-}\right)\left(-\frac{ig}{\sqrt{2}}(\tilde{\ell}_{\rm L}^{\dagger}\partial^{\nu}\tilde{\nu}_{\rm L}-\tilde{\nu}_{\rm L}\partial^{\nu}\tilde{\ell}_{\rm L}^{\dagger})W_{\nu}^{+}\right)\right]\right| d\bar{u}\rangle.$$

In reducing the sleptons in the final state, we get the derivative of the sneutrino (charged slepton) wave function $\exp(i\tilde{\nu}\cdot x)$ ($\exp(i\tilde{\ell}_{\rm L}\cdot x)$) which gives an i times the momentum factors in the amplitude. The contraction of the $W$ fields gives us the $W$ propagator and, as before, integration over the spacetime points where the interactions occur give us momentum conservation at each vertex. We are then left with the matrix element

$$\mathcal{M} = -\frac{1}{2}g^2\bar{v}(\bar{u})\gamma^{\mu}\frac{1-\gamma_5}{2}u(d)D_W(\hat{s})(\tilde{e}_{\rm L}-\tilde{\nu}_{\rm L})_{\mu}, \tag{12.12}$$

which is now straightforward to square to obtain the differential cross section listed in (A.14).[6] The cross sections for the charged slepton (including stau) and sneutrino pair production processes can be similarly obtained and are given in (A.15a)–(A.15b). Note that the cross sections for the production of the first two generations of charged sleptons and sneutrinos are completely determined by their masses, and so are model-independent. For staus, model dependence enters via the stau mixing angle.

In Fig. 12.9, we show slepton pair production cross sections as a function of slepton mass for the Fermilab Tevatron and for the CERN LHC.[7] These results include next-to-leading order corrections (mentioned below) in the limit of very heavy squark masses. The negative results of slepton searches at LEP2 require $m_{\tilde{e}}$ ($m_{\tilde{\mu}}$) to be greater than about 100 (85) GeV. In the region $m_{\tilde{\ell}} \simeq 100$–$200$ GeV, the cross sections for the Fermilab Tevatron are always below 100 fb, and simulation studies indicate that sleptons beyond the reach of LEP2 would be very difficult to detect.[8] Detection of slepton pairs via their direct production seems possible at the CERN LHC if slepton masses are below $\sim$ 300–400 GeV.

[6] Instead of writing this as a differential cross section $d\sigma/dz$ as before, we have written it as a differential cross section over the Mandelstam variable $\hat{t} = (d-\tilde{\ell})^2$ using

$$\frac{d\sigma}{d\hat{t}} = \frac{1}{16\pi\hat{s}^2}\frac{1}{12}|\mathcal{M}|^2,$$

where the factor $1/12$ comes from color and spin averaging over the initial state.

[7] Sometimes in the subsequent discussion of sparticle pair production, we will for convenience use $\tilde{\ell}$ to collectively denote both sleptons and antisleptons, or $\tilde{q}$ to denote both squarks and antisquarks. It should be clear from the context when this occurs.

[8] H. Baer *et al.*, *Phys. Rev.* **D49**, 3283 (1994).

https://doi.org/10.1017/9781009289801.013 Published online by Cambridge University Press

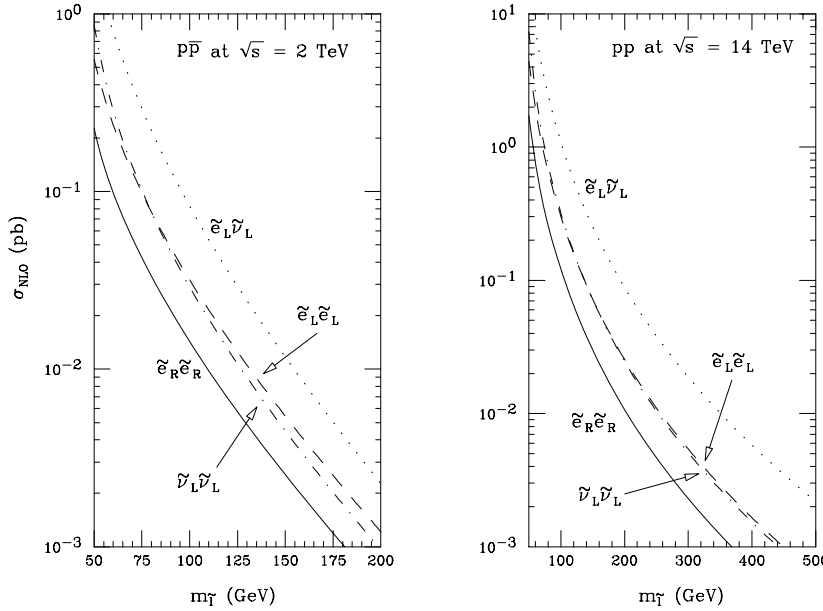


Figure 12.9 Cross sections for production of slepton pairs at the Tevatron and the CERN LHC.

### *12.1.5 Production of gluinos and squarks*

Gluino and squark production at hadron colliders occurs dominantly via strong interactions. Thus, their production rate may be expected to be considerably larger than that for sparticles with just electroweak interactions whose production we have been considering up to now. This is tempered by the fact that in many models colored sparticles are expected to be the heaviest of all the superparticles, so that their production may be kinematically suppressed.

Gluino production at hadron colliders mainly occurs via the diagrams listed in Fig. 12.10. Since the gluon luminosity in hadron collisions falls off rapidly with $\hat{s}$, gluino production from the $gg$ initial state is usually dominant for lower values of $m_{\tilde{g}}$, while $q\bar{q}$ annihilation dominates if $m_{\tilde{g}}$ is large. The differential cross sections for gluino pair production by $gg$ scattering and by $q\bar{q}$ scattering is given by (A.5a) and (A.5b), respectively.[9] Gluino pair production leads to a large rate for multi-jet events with apparent $E_{\mathrm{T}}^{\mathrm{miss}}$ carried off by the daughter LSPs from the decay of the gluinos. Other distinctive gluino signatures will be discussed in subsequent chapters.

[9] The derivative coupling at the three gluon vertex can be handled as explained in the previous subsection. In the present case, the derivative may also act on the gluon propagator but this can be dealt with exactly as before.

https://doi.org/10.1017/9781009289801.013 Published online by Cambridge University Press

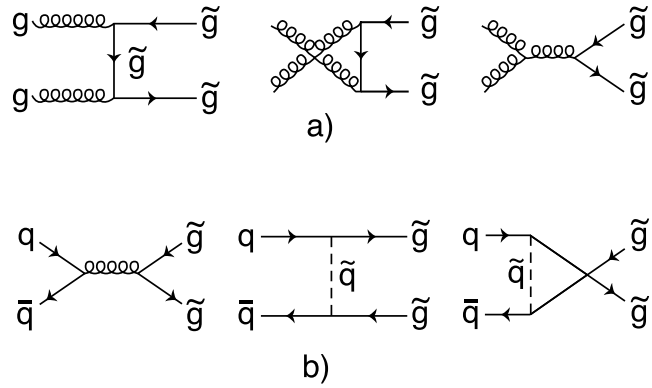


Figure 12.10 Feynman diagrams for leading order gluino pair production processes at hadron colliders.

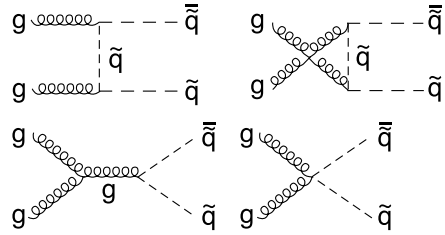


Figure 12.11 Feynman diagrams for squark pair production via gluon scattering at hadron colliders.

Pair production of squarks via $gg$ scattering takes place via the diagrams listed in Fig. 12.11. These scattering reactions lead to particle–antiparticle pairs of the same flavor and type, e.g. $\tilde{u}_L\bar{\tilde{u}}_L$, $\tilde{u}_R\bar{\tilde{u}}_R$, etc. This is also true for $t$-squark pair production: only $\tilde{t}_i\bar{\tilde{t}}_i$ $(i = 1, 2)$ pairs can be produced because gluons do not couple to $\tilde{t}_1\bar{\tilde{t}}_2$ pairs. In addition, as shown in Fig. 12.12, squark pairs can also be produced via quark–quark or quark–antiquark scattering. These contributions are important only for those flavors with significant luminosity in the colliding hadron beams. Not only do different Feynman diagrams contribute to the production of different flavors and types of squarks, as we will see in the next chapter these different squarks have their distinct decay patterns. Thus the cross section magnitudes, angular distributions, and the final decay products all depend on which pair of squarks is being produced. For simulations of superparticle production at colliders it is, therefore, important to separate out the production of different types of squark pairs. The component

https://doi.org/10.1017/9781009289801.013 Published online by Cambridge University Press

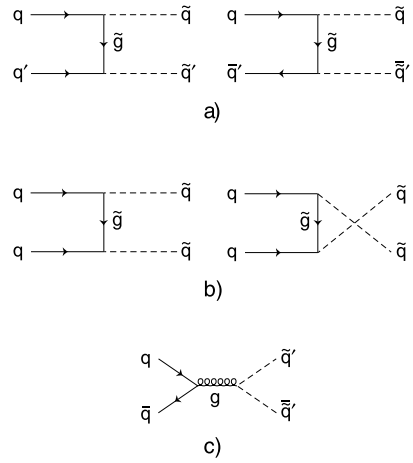


Figure 12.12 Feynman diagrams for squark pair production via quark scattering at hadron colliders.

reactions are

$$q_1\bar{q}_2 \to \tilde{q}_{1\mathrm{L}}\bar{\tilde{q}}_{2\mathrm{R}} \quad \text{and} \quad q_1\bar{q}_2 \to \tilde{q}_{1\mathrm{R}}\bar{\tilde{q}}_{2\mathrm{L}}, \tag{12.13a}$$

$$q_1\bar{q}_2 \to \tilde{q}_{1\mathrm{L}}\bar{\tilde{q}}_{2\mathrm{L}} \quad \text{and} \quad q_1\bar{q}_2 \to \tilde{q}_{1\mathrm{R}}\bar{\tilde{q}}_{2\mathrm{R}}, \tag{12.13b}$$

$$q_1q_2 \to \tilde{q}_{1\mathrm{L}}\tilde{q}_{2\mathrm{R}} \quad \text{and} \quad q_1q_2 \to \tilde{q}_{1\mathrm{R}}\tilde{q}_{2\mathrm{L}}, \tag{12.13c}$$

$$q_1q_2 \to \tilde{q}_{1\mathrm{L}}\tilde{q}_{2\mathrm{L}} \quad \text{and} \quad q_1q_2 \to \tilde{q}_{1\mathrm{R}}\tilde{q}_{2\mathrm{R}}, \tag{12.13d}$$

$$q\bar{q} \to \tilde{q}_{\mathrm{L}}\bar{\tilde{q}}_{\mathrm{R}} \quad \text{and} \quad q\bar{q} \to \tilde{q}_{\mathrm{R}}\bar{\tilde{q}}_{\mathrm{L}}, \tag{12.13e}$$

$$q\bar{q} \to \tilde{q}_{\mathrm{L}}\bar{\tilde{q}}_{\mathrm{L}} \quad \text{and} \quad q\bar{q} \to \tilde{q}_{\mathrm{R}}\bar{\tilde{q}}_{\mathrm{R}}, \tag{12.13f}$$

$$q\bar{q} \to \tilde{q}'_{\mathrm{L}}\bar{\tilde{q}}'_{\mathrm{L}} \quad \text{and} \quad q\bar{q} \to \tilde{q}'_{\mathrm{R}}\bar{\tilde{q}}'_{\mathrm{R}}, \tag{12.13g}$$

$$qq \to \tilde{q}_{\mathrm{L}}\tilde{q}_{\mathrm{L}} \quad \text{and} \quad qq \to \tilde{q}_{\mathrm{R}}\tilde{q}_{\mathrm{R}}, \tag{12.13h}$$

$$q\bar{q} \to \tilde{q}_{\mathrm{L}}\bar{\tilde{q}}_{\mathrm{R}} \quad \text{and} \quad q\bar{q} \to \tilde{q}_{\mathrm{R}}\bar{\tilde{q}}_{\mathrm{L}}. \tag{12.13i}$$

The differential cross sections for these various squark pair production reactions are listed in (A.7a)–(A.7j) of Appendix A. While most of the necessary amplitudes can be straightforwardly calculated using techniques that we have already described, in the evaluation of the amplitude for the processes $q_1q_2 \to \tilde{q}_{1\mathrm{L}}\tilde{q}_{2\mathrm{R}}$ which occur via gluino exchanges in the $t$-channel, and also $u$-channel if $q_1 = q_2$, (see Fig. 12.12) we encounter a new complication. The relevant amplitude depends on the matrix element

$$\langle \tilde{q}_{1\mathrm{L}c}\tilde{q}_{2\mathrm{R}d}| - 2g_s^2 T\left[\left(\tilde{q}_{\mathrm{L}}^{\dagger}\frac{\bar{\tilde{g}}_A\lambda_A}{2}\frac{1-\gamma_5}{2}q\right)(x)\left(\tilde{q}_{\mathrm{R}}^{\dagger}\frac{\bar{\tilde{g}}_B\lambda_B}{2}\frac{1+\gamma_5}{2}q\right)(y)\right]|q_{1a}q_{2b}\rangle,$$

https://doi.org/10.1017/9781009289801.013 Published online by Cambridge University Press

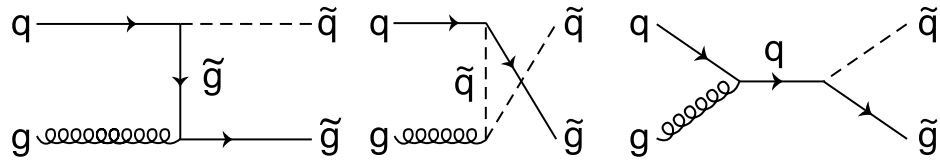


Figure 12.13 Feynman diagrams for leading order gluino–squark associated production at hadron colliders.

where $a$–$d$ are color indices. Reducing the particles in the external states leaves us with,

$$-2g_s^2\langle 0|T\left[\left(e^{i\tilde{q}_{1L}\cdot x}(\frac{\bar{\tilde{g}}_A(x)\lambda_A}{2})_{ca}\frac{1-\gamma_5}{2}u(q_1)e^{-iq_1\cdot x}\right)\right.$$
$$\left.\times\left(e^{i\tilde{q}_{2R}\cdot y}(\frac{\bar{\tilde{g}}_B(y)\lambda_B}{2})_{db}\frac{1+\gamma_5}{2}u(q_2)e^{-iq_2\cdot y}\right)\right]|0\rangle. \qquad (12.14a)$$

We now see that because we have two Dirac-conjugated gluino fields, the vacuum expectation value of their time-ordered product is *not* the Feynman propagator for the gluino. To bring it to this form, we recall that the Majorana nature of the gluino means that the spinor $\tilde{g} \equiv \lambda_A \tilde{g}_A/2$ is a Majorana spinor so that,

$$\bar{\tilde{g}}(x)\frac{1-\gamma_5}{2}u(q_1) = \tilde{g}(x)^T C\frac{1-\gamma_5}{2}C\bar{v}(q_1)^T = -\bar{v}(q_1)\frac{1-\gamma_5}{2}\tilde{g}(x).$$

If we substitute this into (12.14a), we see that the matrix element contains the gluino propagator as expected, but that we obtain a $v$-spinor for the wave function of the quark $q_1$.[10] As usual, we can now write the gluino propagator as a Fourier integral over the four-momentum $p_{\tilde{g}}$; also, integration over the co-ordinates $x$ and $y$ gives four-momentum conservation at each vertex, and the matrix element for $q_1q_2 \to \tilde{q}_{1L}\tilde{q}_{2R}$ reduces to,

$$\mathcal{M} = 2g_s^2\bar{v}(q_1)\frac{1-\gamma_5}{2}(\frac{\lambda_A}{2})_{ca}\frac{1}{(\not{p}_{\tilde{g}} - m_{\tilde{g}})}(\frac{\lambda_A}{2})_{db}\frac{1+\gamma_5}{2}u(q_2), \qquad (12.14b)$$

which can be now squared using usual trace techniques.

Finally, gluinos and squarks may also be produced in association with each other via gluon–quark scattering, as shown in Fig. 12.13. The corresponding cross section is given by (A.6).

[10] This is equivalent to saying that we write the Lagrangian at point $x$ in terms of the anti-quark field, i.e. a field $\psi_{\bar{q}}$ that destroys an antiquark in the initial state or creates a quark in the final state, and the "anti-gluino" field. The reader may also recall that we encountered a similar manipulation in Chapter 3, when we examined the quadratic divergences in the corrections to the two-point function of the field $A$. See also Eq. (3.37a) and (3.37b).

https://doi.org/10.1017/9781009289801.013 Published online by Cambridge University Press

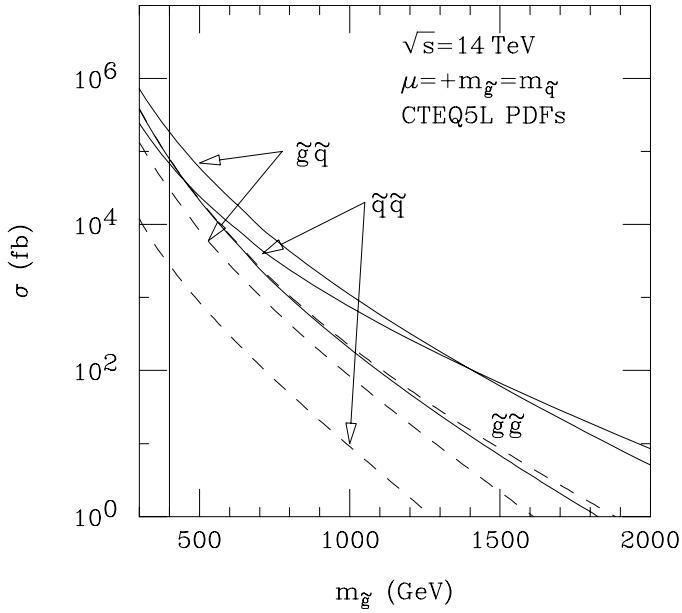


Figure 12.14 Cross sections for squark and gluino production at the CERN LHC $pp$ collider for $m_{\tilde{q}} = m_{\tilde{g}}$ (solid) and for $m_{\tilde{q}} = 2m_{\tilde{g}}$ (dashes).

It is worth emphasizing that because there are no third generation partons in the initial state, squark and gluino production rates are fixed by SUSY QCD in terms of just the squark and gluino masses, and do not depend upon the details of any model. In Fig. 12.14, we show sample cross sections for gluino and squark pair production at the CERN LHC, assuming six flavors of mass degenerate left- and right-squarks. In this example, we take $m_{\tilde{q}} = m_{\tilde{g}}$ (solid lines) and $m_{\tilde{q}} = 2m_{\tilde{g}}$ (dashed lines). The renormalization and factorization scale is chosen to be half the average mass of the sparticles produced, which yields results in accord with next-to-leading order predictions. For the case of $m_{\tilde{q}} = m_{\tilde{g}}$, $\tilde{g}\tilde{q}$ associated production dominates over most of the range of $m_{\tilde{g}}$, until $\tilde{q}\tilde{q}$ pair production dominates at the highest values of $m_{\tilde{g}}$. This behavior is in part a reflection of the PDFs, where production via gluons is dominant for small $x$ values, but production via valence quark scattering dominates for large $x$ values and large sparticle masses. In the case of $m_{\tilde{q}} = 2m_{\tilde{g}}$, $\tilde{g}\tilde{g}$ production is dominant, since these are the lightest mass pairs of sparticles. We see that even for gluinos as heavy as 1 TeV, $\mathcal{O}(10^3$–$10^4)$ gluino and squark events are expected at the LHC for an integrated luminosity of just 10 fb$^{-1}$. It is in this sense that the LHC will be a sparticle factory.

https://doi.org/10.1017/9781009289801.013 Published online by Cambridge University Press

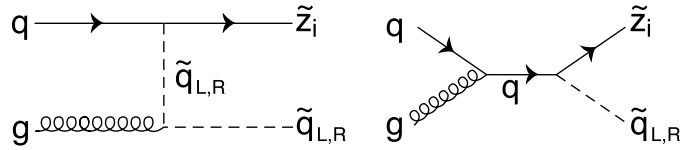


Figure 12.15 Feynman diagrams for leading order squark–neutralino associated production at hadron colliders.

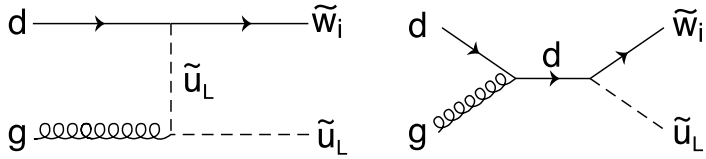


Figure 12.16 Feynman diagrams for leading order squark–chargino associated production at hadron colliders.

**Exercise** *The reader will have noticed that gluinos can be produced only from $gg$ and $q\bar{q}$ initial states, but not from the $qq$ initial state. Argue that this must be the case by color symmetry. Use the reduction of $SU(3)$ tensor products,*

$$\mathbf{3} \otimes \mathbf{3} = \mathbf{3}^* \oplus \mathbf{6},$$
$$\mathbf{8} \otimes \mathbf{8} = \mathbf{1} \oplus \mathbf{8} \oplus \mathbf{8} \oplus \mathbf{10} \oplus \mathbf{10}^* \oplus \mathbf{27},$$

*to make the argument.*

### 12.1.6 Gluino or squark production in association with charginos or neutralinos

Gluinos and squarks may also be produced in association with charginos and neutralinos in a semi-strong reaction. Diagrams leading to squark production in association with neutralinos (charginos) are shown in Fig. 12.15 (Fig. 12.16). These reactions occur by quark–gluon scattering via $u$- and $s$-channel graphs, with cross sections given by (A.8)–(A.10). Sample reaction rates for the CERN LHC are shown in Fig. 12.17 versus $m_{\tilde{g}}$ for $\mu = m_{\tilde{g}} = m_{\tilde{q}}$, $\tan\beta = 5$, and assuming gaugino mass unification and degenerate squarks.

Feynman diagrams for gluino production in association with neutralinos (charginos) are shown in Fig. 12.18 (Fig. 12.19). In this case, production occurs via quark–antiquark scattering via $t$- and $u$-channel squark exchange. The relevant cross sections are given by (A.11)–(A.12). Example cross sections for the LHC are shown in Fig. 12.20 for the same parameters as in Fig. 12.17.

https://doi.org/10.1017/9781009289801.013 Published online by Cambridge University Press

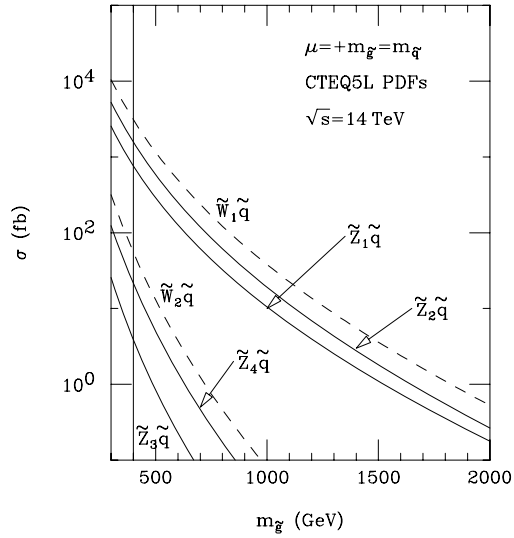


Figure 12.17 Cross sections for chargino or neutralino production in association with squarks at the CERN LHC $pp$ collider for $\tan\beta = 5$, and assuming gaugino mass unification at $M_{\rm GUT}$ and degenerate squarks.

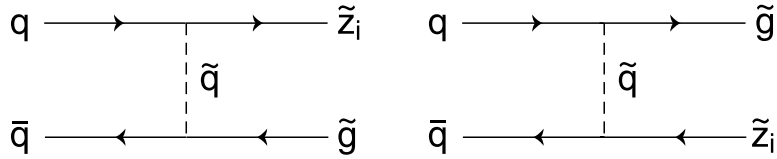


Figure 12.18 Feynman diagrams leading to gluino plus neutralino production at hadron colliders.

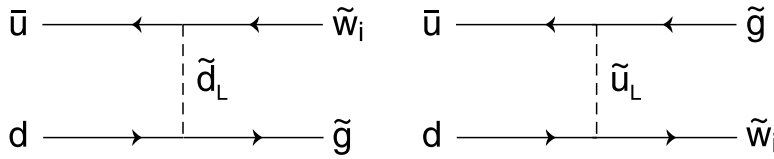


Figure 12.19 Feynman diagrams leading to gluino plus chargino production at hadron colliders.

Generally, the rates for all semi-strong associated production reactions are smaller than rates for direct pair production of gluinos and squarks at the LHC, or to chargino and neutralino pair production at the Fermilab Tevatron. The signatures are not especially distinctive from those arising from cascade decays of gluino and squark pair production, so that these processes appear to be less important for the search for supersymmetry.

https://doi.org/10.1017/9781009289801.013 Published online by Cambridge University Press

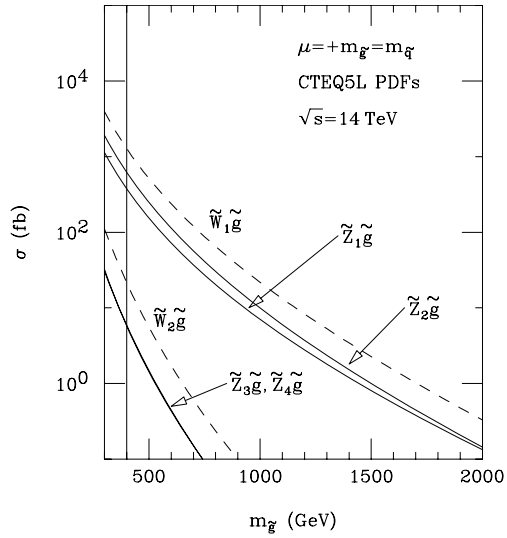


Figure 12.20 Cross sections for chargino or neutralino production in association with gluinos at the CERN LHC $pp$ collider for $\tan\beta = 5$, and assuming gaugino mass unification at $M_{\rm GUT}$.

### 12.1.7 Higher order corrections

Next-to-leading order (NLO) QCD corrections to scattering cross sections are necessary to improve the accuracy of numerical predictions, and such calculations have been carried out for all the sparticle production mechanisms discussed above. The accuracy of leading order (LO) predictions can be ascertained by varying the renormalization and factorization scales inherent in the cross section calculations. For simplicity, we set these two scales equal to each other, and denote them by $Q$. In Fig. 12.21*a*, we show the variation of LO and NLO calculations of $\widetilde{W}_1\widetilde{Z}_2$ production at the CERN LHC with respect to variation in the scale choice, expressed as a ratio with the average mass of the produced sparticles. The uncertainty of the LO result is $\sim 30\%$, while the scale variation of the NLO result is minimal. Typically, for this reaction, the NLO result represents an enhancement of 20%–50%.

In Fig. 12.21*b*, the cross section variation versus scale choice is shown for gluino pair production. In this case, the LO cross section varies by a factor of $\sim 3$, while the NLO result varies only by about 30%. As noted above, for strongly produced SUSY particles a scale choice of 0.3–0.5 times the average sparticle mass will yield LO cross section predictions in accord with NLO results.[11]

[11] NLO sparticle pair production cross sections can be generated by the computer program PROSPINO: see W. Beenakker, R. Höpker and M. Spira, hep-ph/9611232.

https://doi.org/10.1017/9781009289801.013 Published online by Cambridge University Press

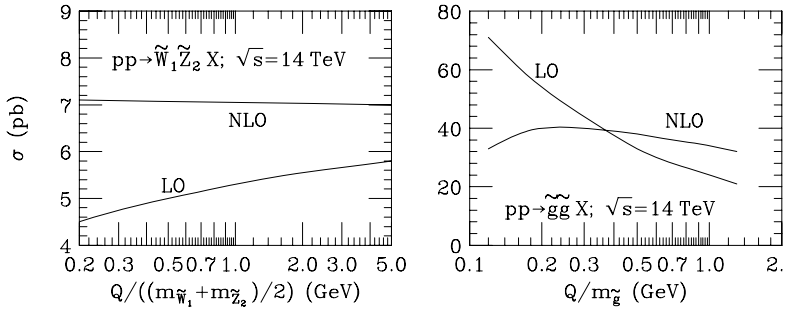


Figure 12.21 Cross sections for (a) chargino plus neutralino production for the mSUGRA framework with $m_0 = 100$ GeV, $m_{1/2} = 150$ GeV, $A_0 = 300$ GeV, $\tan\beta = 4$, and $\mu > 0$; the figure is adapted from W. Beenakker *et al.*, *Phys. Rev. Lett.* **83**, 3780 (1999). In (b), gluino pair production versus variation in renormalization/factorization scale is shown at the CERN LHC $pp$ collider; this figure is adapted from W. Beenaker *et al.*, *Nucl. Phys.* **B492**, 51 (1997).

### *12.1.8 Sparticle production at the Tevatron and LHC*

In Fig. 12.22, we show total cross sections for production of supersymmetric particles at the Fermilab Tevatron, for $p\bar{p}$ collisions at $\sqrt{s} = 2$ TeV, as a function of the physical gluino mass, assuming the squarks are all degenerate. In frame (a), for $m_{\tilde{q}} = m_{\tilde{g}}$, we see that chargino and neutralino production is the dominant production mechanism over the entire range of $m_{\tilde{g}}$ values shown. Strong production of gluinos and squarks never dominates, mainly because in this case the gluino and squark masses are so heavy compared to the charginos and neutralinos.[12] In frame (b), we show the corresponding cross sections for $m_{\tilde{q}} = 2m_{\tilde{g}}$. In this case, strong production cross sections are even more suppressed due to large squark masses, and production of charginos and neutralinos is dominant. We see that $\widetilde{W}_1^+\widetilde{W}_1^-$ and $\widetilde{W}_1^\pm\widetilde{Z}_2$ production processes dominate sparticle production at the Tevatron.

Figure 12.23 illustrates sparticle production rates at the CERN LHC. In frame (*a*) for $\mu = m_{\tilde{g}} = m_{\tilde{q}}$, gluino and squark production dominates unless gluinos and squarks are heavier than 1.7 TeV, in which case chargino and neutralino production has the largest rate. For the heavy squark case in frame (*b*), gluino and squark production is dominant for $m_{\tilde{g}} \lesssim 800$ GeV. Associated production is never dominant.

## 12.2 Sparticle production at $e^+e^-$ colliders

Since superpartners were not discovered at the CERN LEP2 $e^+e^-$ collider, operating at $\sqrt{s} \simeq 200$ GeV, it seems likely that if weak scale supersymmetry exists

[12] This is not the case for $\mu = -m_{\tilde{g}}$ for which charginos and neutralinos tend to be heavier. Then strong production is dominant if $m_{\tilde{g}} \lesssim 300$ GeV (200 GeV) for $m_{\tilde{q}} = m_{\tilde{g}}$ ($m_{\tilde{q}} = 2m_{\tilde{g}}$).

https://doi.org/10.1017/9781009289801.013 Published online by Cambridge University Press

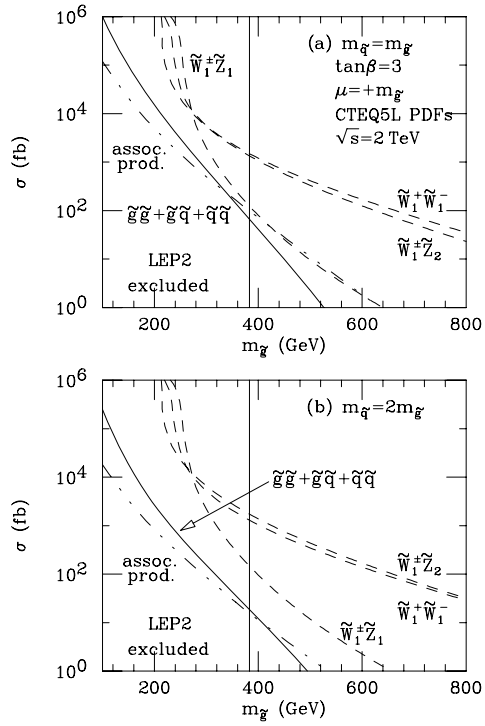


Figure 12.22 Cross sections for the production of gluinos, squarks, charginos, and neutralinos at the Fermilab Tevatron $p\bar{p}$ collider. We assume gaugino mass unification at $Q = M_{\rm GUT}$, and also that all squarks have the same mass. To the left of the vertical line, the chargino is lighter than 100 GeV.

in nature, its discovery will take place at a hadron machine. Nevertheless, there is considerable interest in the construction of a linear $e^+e^-$ collider to operate in the energy regime of $\sqrt{s} \sim 0.5$–$1.5$ TeV. Despite the lower energy, the advantages of such a machine (over hadron colliders) for the elucidation of weak scale supersymmetry are numerous:

- Unlike at hadron colliders where the energy available for the production of new particles is limited to that of the colliding partons, essentially all of the available center of mass energy may go into creating new states at an $e^+e^-$ collider. This is because, unlike hadrons, electrons and positrons are elementary particles.
- For the same reason, the $e^+e^-$ initial state has a well-defined energy and momentum, and allows detailed kinematic reconstruction of scattering events, facilitating precision measurements. Again for this same reason, $e^+e^-$ scattering events are very clean because the hard scattering event is free of contamination from spectator jets and initial state QCD radiation that are necessarily present in hadron

https://doi.org/10.1017/9781009289801.013 Published online by Cambridge University Press

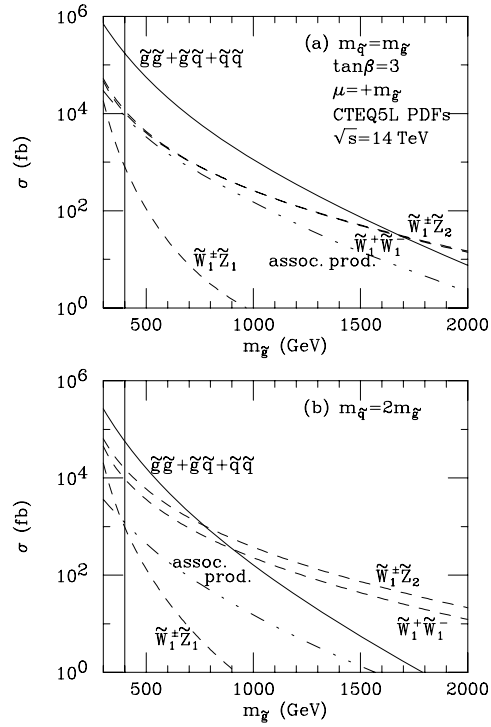


Figure 12.23 Cross sections for gluinos, squarks, charginos and neutralinos at the CERN LHC $pp$ collider. As in Fig. 12.22, we assume gaugino mass unification and the degeneracy of squarks. The chargino is lighter than 100 GeV to the left of the vertical line.

scattering. The clean environment together with the simplicity of the initial state allows final states to be reconstructed with greater precision.

- Aside from kinematic suppression, all particles with non-trivial $SU(2)_{\rm L} \times U(1)_{\rm Y}$ quantum numbers are produced at comparable rates so that signal to background is never very small.
- The availability of a longitudinally polarized electron, and possibly also a positron, beam is a novel feature of electron–positron colliders. Since SUSY signals and SM backgrounds are both sensitive to beam polarization, polarized beams can be a very valuable tool, both for reducing SM backgrounds and for separating SUSY reactions from one another.
- The beam energy is tunable. Together with beam polarization capability, this will allow experimentalists to isolate particular SUSY processes, further facilitating determination of sparticle properties.

The biggest physics advantages of hadron colliders are (a) the higher beam energy, which makes them an ideal facility for a broad band search for new physics,

https://doi.org/10.1017/9781009289801.013 Published online by Cambridge University Press

and (b) the sizable cross section for SUSY processes which results in observable signal rates for luminosity and energy which is supposed to be well within the realm of current technology. In contrast, both signal and background cross sections tend to be small at high energy $e^+e^-$ colliders, so that very high beam intensities are essential for physics. Thus, while sparticles may be discovered at a hadron collider, and many of their properties determined there, a TeV scale $e^+e^-$ collider operating with polarizable beams will allow a systematic program of precision studies of all the superparticles with significant production cross sections.

### *12.2.1 Production of sleptons, sneutrinos, and squarks*

Pair production of smuons, staus, and their corresponding sneutrinos takes place via the same Feynman diagrams as in Fig. 12.7, with $q\bar{q}$ replaced by $e^-e^+$. Squark pairs are also produced via the same Feynman diagrams as for charged slepton production, with the sleptons replaced by squarks. The relevant matrix elements can be evaluated as before. The one new element is that, for reasons explained at the start of this chapter, we present the cross sections for polarized electron/positron beams. This simply entails inserting corresponding chiral projectors $P_{\rm L/R} = \frac{1\mp\gamma_5}{2}$ to select out the desired polarization in front of the initial state electron/positron spinor wave functions when evaluating the various amplitudes.[13] The cross sections for squark pair production, as well as for charged sleptons and sneutrinos of the first two generations, are given by (A.21a)–(A.21c). The cross section for unpolarized beams, or for partially polarized beams, can be obtained from these using (A.28). We note that for the first two generations of squarks as well as for smuon and sneutrino production, the cross sections are determined by just the sfermion mass (together with known SM parameters), and so are model-independent.

In Fig. 12.24, we show the cross section for smuon and sneutrino ($\tilde{\nu}_\mu$ or $\tilde{\nu}_\tau$) pair production from unpolarized beams as a function of the sparticle mass, for an $e^+e^-$ collider operating at $\sqrt{s} = 1$ TeV. The stau cross section depends on the stau mixing angle but typically has a similar magnitude. Linear colliders are currently being designed, and the projected luminosity for such a machine might be 10–50 fb$^{-1}$ per year, or larger. The Technical Design Report of the TESLA collider being considered for construction quotes a luminosity of $3.4 \times 10^{34}$ cm$^{-2}$s$^{-1}$ at $\sqrt{s} = 500$ GeV, corresponding to a projected design luminosity in excess of 300 fb$^{-1}$/yr, assuming the machine runs about a third of the time. Depending on the luminosity that is ultimately attained, several hundred to several thousand smuon pair events might be expected annually for smuon masses heavy enough to be within 80% of the kinematic limit.

[13] At the energies of interest it is safe to neglect the electron mass so that there is no difference between chirality and helicity.

https://doi.org/10.1017/9781009289801.013 Published online by Cambridge University Press

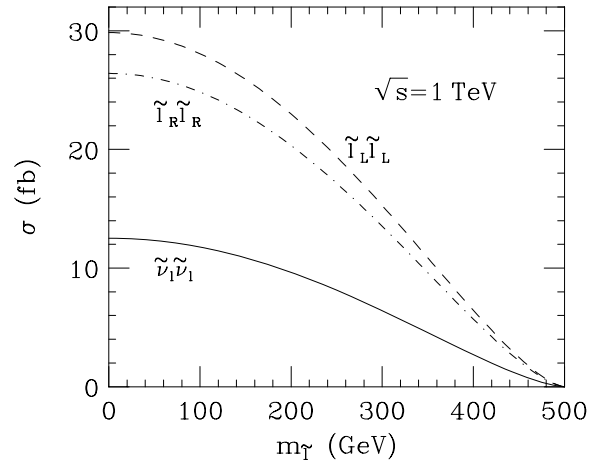


Figure 12.24 Cross sections for production of smuons and associated sneutrinos at a $\sqrt{s} = 1$ TeV $e^+e^-$ collider with unpolarized beams.

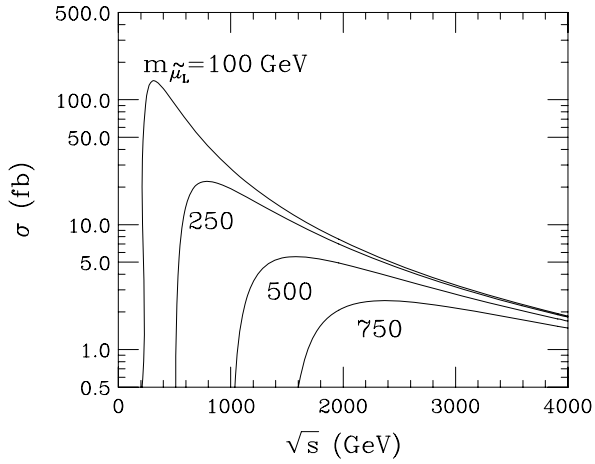


Figure 12.25 Cross sections for left-smuon pair production versus $\sqrt{s}$ for various smuon masses at an $e^+e^-$ collider with unpolarized beams.

The variation of this cross section versus collider $\sqrt{s}$ is shown in Fig. 12.25, for various smuon masses. Slightly above threshold, the cross section attains a maximum, falling off as the energy escalates. The rapid rise of the cross section close to the kinematic end-point is characteristic of the $\beta^3$ $p$-wave threshold behavior evident in (A.21a).

The cross sections for various squark pair production processes as a function of squark mass are shown in Fig. 12.26 for a 1 TeV $e^+e^-$ collider with unpolarized beams. For third generation squarks, as for staus, the cross sections will be modified

https://doi.org/10.1017/9781009289801.013 Published online by Cambridge University Press

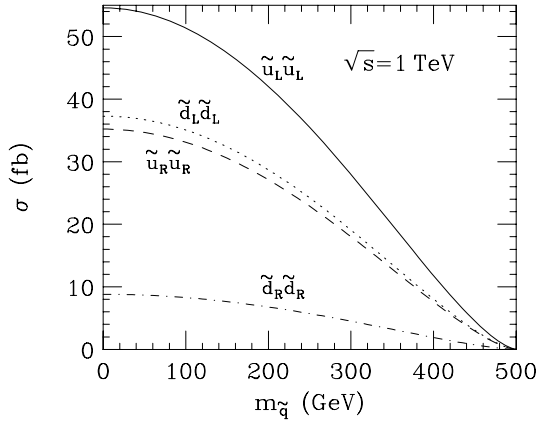


Figure 12.26 Cross sections for various types of squark pairs at a 1 TeV $e^+e^-$ collider with unpolarized beams, versus $m_{\tilde{q}}$.

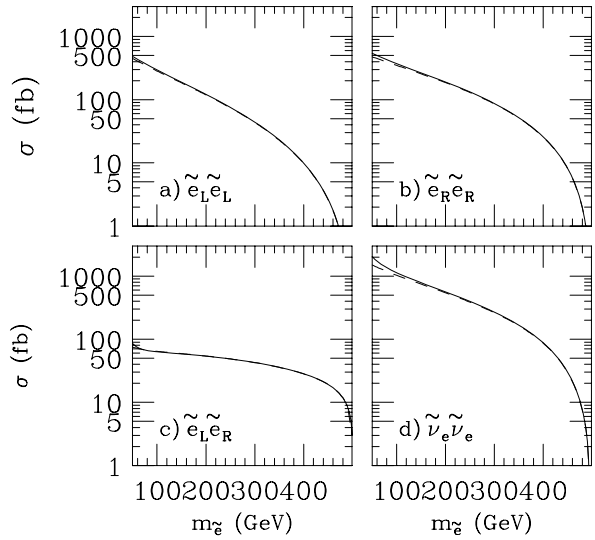


Figure 12.27 Cross sections for producing left- and right-selectron and electron sneutrinos at a $\sqrt{s} = 1$ TeV $e^+e^-$ collider with unpolarized beams, versus the corresponding selectron or sneutrino mass for the parameters listed in the text. The solid (dashed) lines correspond to positive (negative) values of $\mu$.

by mixing angle factors. Production of left-squarks is the largest of these cross sections. We note that these cross sections are much smaller than the corresponding cross sections at the LHC.

The mechanisms for the production of first generation sleptons and sneutrinos are more complicated. In addition to the first of the Feynman graphs of Fig. 12.7,

https://doi.org/10.1017/9781009289801.013 Published online by Cambridge University Press

left- and right-selectron pairs may also be produced via the exchange of any of the neutralinos in the $t$-channel. Thus $\sigma(\tilde{e}_L\tilde{e}_L)$ and $\sigma(\tilde{e}_R\tilde{e}_R)$ depend on parameters entering the neutralino mass matrix. Moreover, $\tilde{e}_L\bar{\tilde{e}}_R$ and $\bar{\tilde{e}}_L\tilde{e}_R$ pairs can also be produced but only via these neutralino exchange graphs. Finally, electron sneutrinos may be pair produced either via the $s$-channel $Z$ exchange diagram shown in Fig. 12.7 that is common to all sneutrinos, or by chargino exchange in the $t$-channel.

Production cross sections for selectron and sneutrino pair production are illustrated in Fig. 12.27 versus selectron or sneutrino mass, for a $\sqrt{s} = 1$ TeV $e^+e^-$ collider. We take $\mu = \pm 2m_{\tilde{\ell}}$ (solid/dashes), $\tan\beta = 5$ and $M_2 = m_{\tilde{\ell}}$, and assume gaugino mass unification. The most striking feature of this figure is that the selectron (sneutrino) pair production cross sections are about 10 (50) times larger than the corresponding cross sections for second generation sleptons. This is because of the $t$-channel contributions to their production. Notice also that for the first generation, aside from possible differences in kinematic factors, electron sneutrinos usually have the largest production cross section. We will see in the next chapter that sneutrinos may decay visibly, so that sneutrino production can be an important discovery mode. Also, the cross section for $\tilde{e}_L\tilde{e}_L + \tilde{e}_R\tilde{e}_R$ production is almost an order of magnitude larger than that for $\tilde{e}_L\tilde{e}_R$ production. Nevertheless, even for a modest integrated luminosity of 20 fb$^{-1}$, $\mathcal{O}(1000)$ $\tilde{e}_L\tilde{e}_R$ events should be expected at a linear collider. This is important because in models where $\tilde{e}_L$ and $\tilde{e}_R$ have very different masses (e.g. GMSB models), $\tilde{e}_L\tilde{e}_R$ production may be the only reaction which gives access to the heavier selectron.

---

**Exercise** *Evaluate the cross section for selectron pair production by electron–electron collisions which takes place via neutralino exchanges in the $t$- and $u$-channels. To obtain the matrix element you will have to perform manipulations similar to those that we performed when we evaluated the cross section for the process $q_1q_2 \to \tilde{q}_{1L}\tilde{q}_{2R}$ in the previous section.*

*Notice that the cross section that you evaluate has a different threshold behavior from that for selectron production in $e^+e^-$ collisions. This, together with the fact that lepton number conservation implies that we have no SM backgrounds from $W^-W^-$ production, suggests that the selectron mass can be more precisely measured via this process than at $e^+e^-$ colliders.*

---

### *12.2.2 Production of charginos and neutralinos*

Production of $\widetilde{W}_1\overline{\widetilde{W}}_1$ and $\widetilde{W}_2\overline{\widetilde{W}}_2$ pairs proceeds via the Feynman diagrams of Fig. 12.3, by replacing $d\bar{d}$ with $e^-e^+$, and $\tilde{u}_L$ by $\tilde{\nu}_{eL}$. The $s$-channel $Z$ exchange

https://doi.org/10.1017/9781009289801.013 Published online by Cambridge University Press

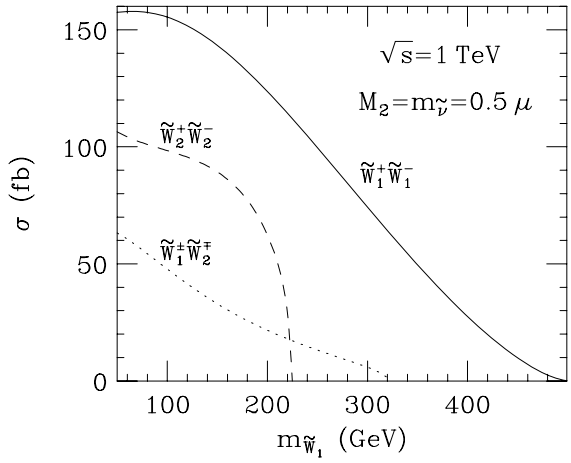


Figure 12.28 Cross sections for chargino pair production at a 1 TeV $e^+e^-$ collider with unpolarized beams, versus $m_{\widetilde{W}_1}$, for $\tan\beta = 5$.

and $t$-channel sneutrino exchange graphs also lead to the production of $\widetilde{W}_2\overline{\widetilde{W}}_1$ and $\widetilde{W}_1\overline{\widetilde{W}}_2$ pairs. The differential cross sections for these various chargino production processes are given by (A.27a)–(A.27d). In many models, $|\mu| \gg M_2$, so that the lighter (heavier) chargino is gaugino-like (higgsino-like). Typically $\sigma(\widetilde{W}_1^+\widetilde{W}_1^-)$ is large because of the enhanced isotriplet coupling of the charginos to $Z^0$. However, this cross section can be sensitive to the sneutrino mass because of the interference between the $s$- and $t$-channel amplitudes which *reduces* the cross section if $\sqrt{s} > M_Z$.

In Fig. 12.28 we illustrate the cross sections versus the lighter chargino mass for various chargino production processes at a $\sqrt{s} = 1$ TeV $e^+e^-$ collider. We take $M_2 = m_{\tilde{\nu}_e} = 0.5\mu$, $\tan\beta = 5$. For $M_2 = 0.5\mu \gg M_W$, $m_{\widetilde{W}_2} \sim 2m_{\widetilde{W}_1}$ and production of heavier chargino pairs is kinematically (as well as dynamically) suppressed relative to that of lighter chargino pairs, and cuts off at the kinematic limit which is close to $2m_{\widetilde{W}_1} \sim m_{\widetilde{W}_2} = 500$ GeV. The mixed process $\widetilde{W}_2\overline{\widetilde{W}}_1 + \widetilde{W}_1\overline{\widetilde{W}}_2$ always occurs at a lower rate. Note, however, that for an integrated luminosity of 100 fb$^{-1}$ there should be several hundred $\widetilde{W}_1^\pm\widetilde{W}_2^\mp$ events beyond the kinematic limit for $\widetilde{W}_2^+\widetilde{W}_2^-$ production.

In many supersymmetric models, $\widetilde{W}_1$ is the lightest of visibly decaying SUSY particles. If charginos are kinematically accessible, they should be produced at observable rates in $e^+e^-$ collisions because of their unambiguous couplings to the photon and to the $Z$. As shown in Fig 12.29, this rate may be significantly smaller than its typical expectation if the sneutrino happens to be relatively light, but should nonetheless be observable.

https://doi.org/10.1017/9781009289801.013 Published online by Cambridge University Press

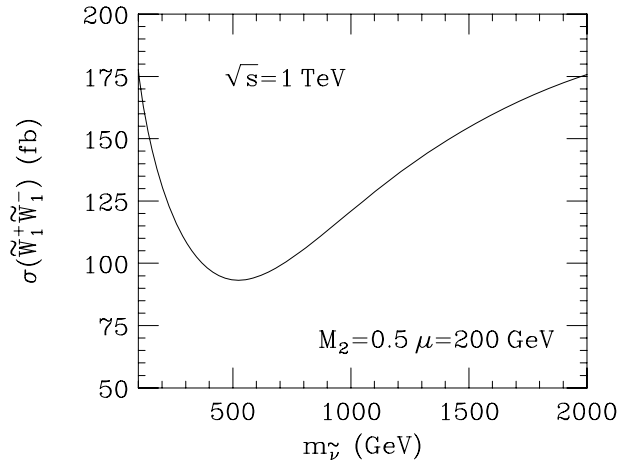


Figure 12.29 Cross sections for chargino pair production processes at a 1 TeV $e^+e^-$ collider with unpolarized beams, versus $m_{\tilde{\nu}_e}$, for $M_2 = 0.5\mu = 200$ and $\tan\beta = 5$.

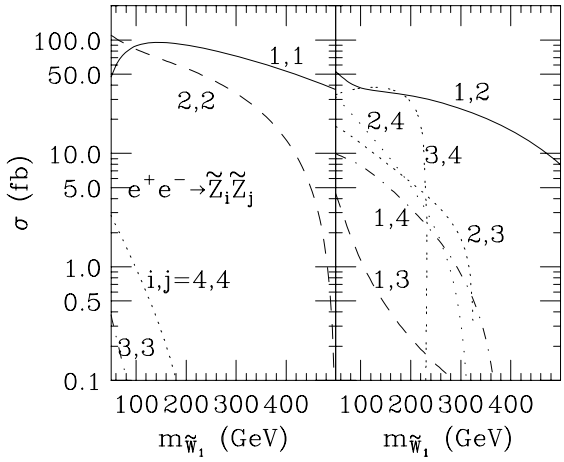


Figure 12.30 Cross sections for neutralino pair production at a 1 TeV $e^+e^-$ collider with unpolarized beams, versus $m_{\tilde{W}_1}$, for $\tan\beta = 5$ and $M_2 = m_{\tilde{e}} = 0.5\mu$.

Neutralino pair production occurs at $e^+e^-$ colliders via the diagrams of Fig. 12.5 with $q\bar{q}$ replaced by $e^-e^+$ and $\tilde{q}_{\rm L,R}$ replaced by $\tilde{e}_{\rm L,R}$. The corresponding differential cross section is given by (A.26). Sample neutralino production cross sections are shown in Fig. 12.30, for the same parameters as in Fig. 12.28 but with $m_{\tilde{\nu}_e}$ replaced by $m_{\tilde{e}_{\rm L}} = m_{\tilde{e}_{\rm R}}$. For the parameters selected, $\widetilde{Z}_1 \simeq \tilde{B}$ and $\widetilde{Z}_2 \simeq \tilde{W}$, so that by $SU(2)_{\rm L} \times U(1)_{\rm Y}$ gauge symmetry, these neutralinos have *small* couplings

https://doi.org/10.1017/9781009289801.013 Published online by Cambridge University Press

to $Z$ bosons,[14] but couple to the $e\tilde{e}_{L,R}$ system via the corresponding *gauge coupling* (since the wino component does not couple to $\tilde{e}_R$, the $e\tilde{e}_R\widetilde{Z}_2$ coupling is small). Since selectrons have been assumed to be relatively light, in this illustration, $t$-channel amplitudes are large: $\widetilde{Z}_1\widetilde{Z}_1$ pair production is large because of the large hypercharge of $\tilde{e}_R$. $\widetilde{Z}_1\widetilde{Z}_2$ production mainly occurs via $\tilde{e}_L$ exchange because $\tilde{e}_L$ couples to both the bino and the wino; however, this rate is smaller than that for $\widetilde{Z}_1\widetilde{Z}_1$ because of the smaller hypercharge of $\tilde{e}_L$ (in addition to kinematic suppression). For the same reason, $\widetilde{Z}_2\widetilde{Z}_2$ production mainly occurs via $\tilde{e}_L$ exchange. The neutralinos $\widetilde{Z}_3$ and $\widetilde{Z}_4$ are mainly higgsino-like, with the magnitude of each higgsino component being close to $\frac{1}{\sqrt{2}}$. Cross sections for $\widetilde{Z}_3\widetilde{Z}_3$ and $\widetilde{Z}_4\widetilde{Z}_4$ pair production are, however, very small because the $Z\widetilde{Z}_{3(4)}\widetilde{Z}_{3(4)}$ coupling in (8.101) is clearly strongly supressed, and the corresponding amplitudes for $t$-channel exchanges are supressed for dynamical reasons. The rate for $\widetilde{Z}_3\widetilde{Z}_4$ production, which mainly occurs via unsuppressed couplings to the $Z$ boson is large, and dominates the kinematically favored (but dynamically suppressed) production of "light–heavy" neutralino pairs.

In $R$-parity conserving models with $\widetilde{Z}_1$ as the LSP, the $\widetilde{Z}_1\widetilde{Z}_1$ final state will be invisible, except for initial state photon radiation. However, as in this example, in mSUGRA and mGMSB models with $m_{\widetilde{Z}_2} \simeq m_{\widetilde{W}_1} \simeq 2m_{\widetilde{Z}_1}$, $\widetilde{Z}_1\widetilde{Z}_2$ production may be observable even if chargino pairs are not kinematically accessible. We should stress though that unlike chargino cross sections that are relatively robust, neutralino production cross sections are very sensitive to model parameters. In particular, if selectrons are very heavy and $|\mu| \gg |M_{1,2}|$ (as is possible in many models), $\widetilde{Z}_1\widetilde{Z}_1$, $\widetilde{Z}_1\widetilde{Z}_2$, and $\widetilde{Z}_2\widetilde{Z}_2$ production mainly occurs via $Z$ exchange through the suppressed higgsino components of the neutralinos: in this case, these production cross sections can be very small even if neutralino production is kinematically unsuppressed.

### 12.2.3 Effect of beam polarization

We have already mentioned that the availability of longitudinally polarized beams at a linear $e^+e^-$ collider serves as a powerful additional tool for signal analysis at these facilities. The degree of longitudinal beam polarization can be parametrized as

$$P_L(e^-) = f_L - f_R, \quad \text{where} \tag{12.15a}$$

$$f_L = \frac{n_L}{n_L + n_R} = \frac{1 + P_L}{2}, \quad \text{and} \tag{12.15b}$$

$$f_R = \frac{n_R}{n_L + n_R} = \frac{1 - P_L}{2}. \tag{12.15c}$$

[14] After all, this is the SUSY analogue of the three neutral vector boson coupling which is forbidden by gauge invariance.

https://doi.org/10.1017/9781009289801.013 Published online by Cambridge University Press

Here, $n_{\rm L,R}$ is the number of left-(right-)polarized electrons in the beam, and $f_{\rm L,R}$ is the corresponding fraction. Thus, a 90% right-polarized beam would correspond to $P_{\rm L}(e^-) = -0.8$, and a completely unpolarized beam corresponds to $P_{\rm L}(e^-) = 0$.

In Appendix A we have collected the various SM and SUSY cross sections for polarized electron and positron beams. In practice, however, beams are always partially polarized, and the relevant cross sections can be obtained using

$$\begin{aligned}\sigma = {} & f_{\rm L}(e^-) f_{\rm L}(e^+)\sigma_{\rm LL} + f_{\rm L}(e^-) f_{\rm R}(e^+)\sigma_{\rm LR} \\ & + f_{\rm R}(e^-) f_{\rm L}(e^+)\sigma_{\rm RL} + f_{\rm R}(e^-) f_{\rm R}(e^+)\sigma_{\rm RR},\end{aligned} \tag{12.16}$$

where $f_{\rm L}$ and $f_{\rm R}$ are defined above, and $\sigma_{ij}$ ($i, j = {\rm L}, {\rm R}$) is the cross section from $e_i^- e_j^+$ annihilation.

In Fig. 12.31, we show the production cross sections for various SM particle pair production processes at an $e^+e^-$ collider operating at $\sqrt{s} = 500$ GeV, versus the electron beam polarization parameter $P_{\rm L}(e^-)$, taking the positrons to be unpolarized. The most striking feature is the strong dependence of the $W$ boson pair production cross section on $P_{\rm L}(e^-)$. This is important because $W^+W^-$ production, which is the SM process with the largest cross section (for unpolarized beams), can lead to events with "missing energy" and "missing momentum" carried off by neutrinos from leptonic decays of $W$, and so is an important background to the SUSY signal. Fortunately, this rate can be reduced to tiny values by using an increasingly right-handed electron beam (see the exercise below). The other SM processes have a less severe dependence on beam polarization, but generally have the largest rates for left-polarized beams.

The polarization dependence of SUSY particle production cross sections is illustrated in Fig. 12.32, for the mSUGRA model with parameters shown in the figure. We see that the production of first generation sleptons, $\widetilde{W}_1$ pairs and some neutralino pairs is strongly sensitive to $P_{\rm L}(e^-)$. By adjusting the polarization of the electron beam, we see that it is possible to select out event samples that are rich in $\tilde{e}_{\rm L}$ or $\tilde{e}_{\rm R}$ (in addition to other sparticles). In addition to the fact that polarization can be used to reduce SM background, this intra-generational separation can also be important for detailed studies of these sparticles. Indeed we will see that electron beam polarization is a very useful tool when engaging in precision studies of the properties of SUSY particles.

While the degree of beam polarization that will be attained at future linear colliders is still uncertain, it is thought that 80%, or higher, polarization for the electron beam will certainly be possible. The situation for positron beams is less clear, but positron beam polarization of about 60% seems to be the target.

https://doi.org/10.1017/9781009289801.013 Published online by Cambridge University Press

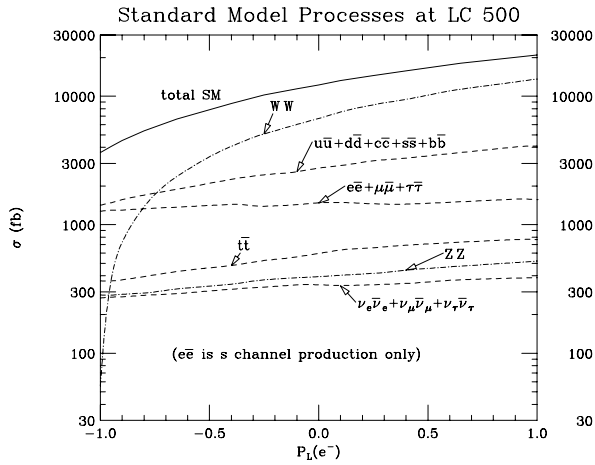


Figure 12.31 Cross sections for various SM pair production processes versus the electron beam polarization parameter $P_{\rm L}(e^-)$, for $e^+e^-$ collisions at $\sqrt{s} = 500$ GeV. We take the positrons to be unpolarized. Reprinted with permission from H. Baer, R. Munroe, and X. Tata, *Phys. Rev*. **D54**, 6735 (1996), copyright (1996) by the American Physical Society.

---

**Exercise** *We saw in Fig. 12.31 that the WW cross section showed a very strong dependence on the electron beam polarization. In view of the importance of eliminating this background, it is worthwhile to understand the smallness of the cross section for* $P_{\rm L}(e^-) = -1$.

(**a**) *Draw the Feynman diagrams by which this process occurs. Since W's couple only to left-handed electrons, it is straightforward to see that the amplitude for the neutrino exchange diagram vanishes if* $P_{\rm L}(e^-) = -1$. *Remember that electron masses are negligible at the energy that we are considering. For a purely right-handed electron beam, this leaves us with just the Z and photon exchange amplitudes.*

(**b**) *To analyze these s-channel amplitudes, it is convenient to work in terms of the original hypercharge and* $SU(2)_{\rm L}$ *gauge bosons rather than in terms of the photon and the Z. Since right-handed electrons have no coupling to the* $SU(2)_{\rm L}$ *gauge boson, the internal vector boson line in the s-channel Feynman diagram must start off as a hypercharge gauge boson at the electron positron vertex. Gauge invariance precludes any coupling between this boson and the* $W^+W^-$ *pair. Thus, this amplitude would vanish but for mixing between the hypercharge and* $SU(2)$ *gauge bosons. This mixing originates in the gauge-covariant kinetic*

https://doi.org/10.1017/9781009289801.013 Published online by Cambridge University Press

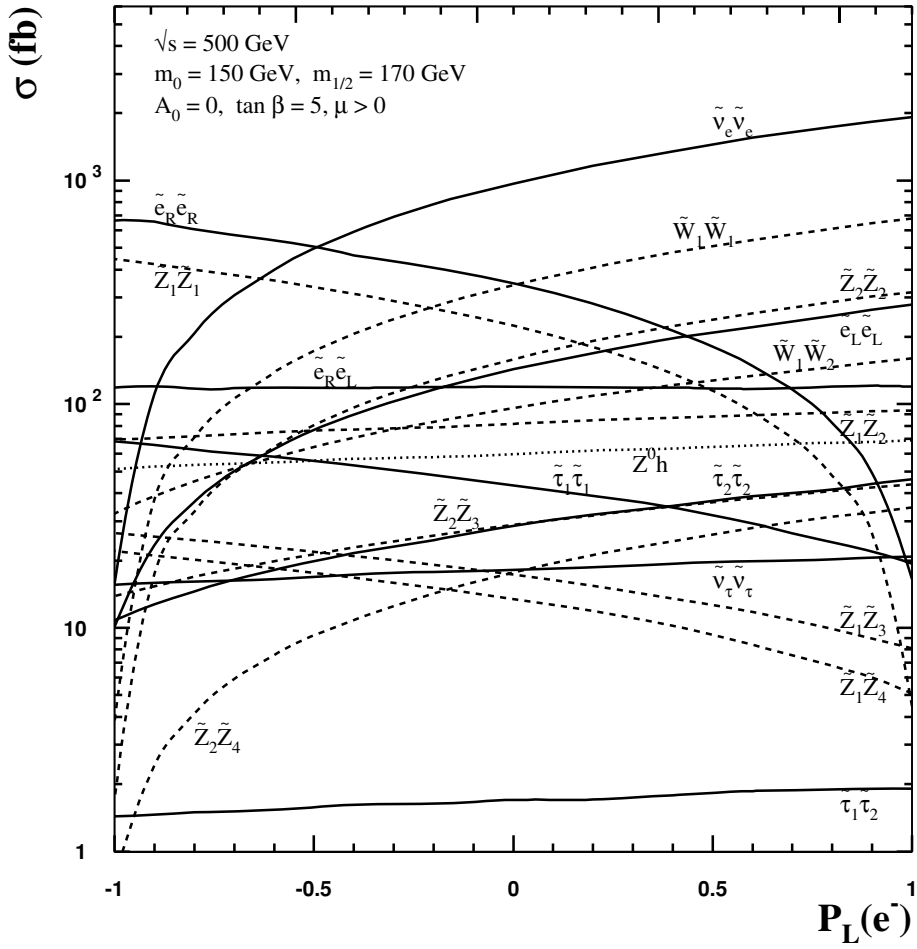


Figure 12.32 Cross sections for production of various sparticle pairs in the mSUGRA model versus the electron beam polarization parameter, for $e^+e^-$ collisions at $\sqrt{s} = 500$ GeV. The positron beam is taken to be unpolarized. Reprinted with permission from H. Baer, C. Balázs, J. K. Mizukoshi and X. Tata, *Phys. Rev* **D63**, 055011 (2001), copyright (2001) by the American Physical Society.

*energy,*

$$|D_\mu \phi|^2 \ni\sim g g' \langle \phi \rangle^2 W_{3\mu} B^\mu,$$

*of the field $\phi$ defined below (8.22b). Use this to show that the $s$-channel amplitude must be proportional to $M_Z^2$. For dimensional reasons it must, therefore, depend on $M_Z^2/s$ and so becomes very small at high energy for right-handed electron beams.*

https://doi.org/10.1017/9781009289801.013 Published online by Cambridge University Press

**Exercise** *Explain the polarization dependence of the slepton and sneutrino pair production cross sections in Fig. 12.32. In particular, explain clearly why stau and tau sneutrino pair production is much less sensitive to $P_L(e^-)$ compared to first generation sleptons.*

### *12.2.4 Bremsstrahlung and beamstrahlung*

Up to now, we have focussed on particle production cross sections at $e^+e^-$ colliders where the full beam energy goes into the hard scattering. However, to properly describe signals and backgrounds to sparticle production at $e^+e^-$ colliders operating in the TeV range, one must allow for forward initial state radiation of high energy photons or bremsstrahlung. An additional complication comes from energy loss due to beam–beam interactions, the so-called beamstrahlung effect. The photons from both these effects are lost down the beam pipe resulting in an unmeasurable loss in the energy of the beam. This reduces the CM energy of the colliding beams, and results in an (unknown) longitudinal momentum for the hard scattering initial state. It is essential to incorporate bremsstrahlung and beamstrahlung losses for precision studies that are possible at linear colliders.

The bremsstrahlung effect can be included by convoluting $e^+e^-$ cross sections with an effective electron structure function. A simple parametrization is the Kuraev–Fadin distribution, given by[15]

$$D_e^{\rm brem}(x, Q^2) = \frac{1}{2}\beta(1-x)^{\frac{\beta}{2}-1}(1+\frac{3}{8}\beta) - \frac{1}{4}\beta(1+x), \tag{12.17a}$$

where

$$\beta \equiv \frac{2\alpha}{\pi}(\ln\frac{Q^2}{m_e^2} - 1), \tag{12.17b}$$

$x$ is the electron fractional momentum, and $Q$ is the scale of hard scattering. The bremsstrahlung distribution is shown by the dashed curve in Fig. 12.33.

In addition, for the very dense, compact electron and positron beams that are essential to obtain the high luminosity needed for high energy linear colliders, one must account for beamstrahlung. In effect, the electron or positron beams are so compact that energy loss can occur due to beam interactions before the hard scattering. This energy loss can be calculated semi-classically, and gives rise to a beamstrahlung distribution function, $D_e^{\rm beam}(x)$. A parametrization of the beamstrahlung distribution function is too complicated to present here, but it does depend on machine characteristics and beam profile. Stipulating a beamstrahlung

[15] E. Kuraev and V. Fadin, *Sov. J. Nucl. Phys.* **41**, 466 (1985).

https://doi.org/10.1017/9781009289801.013 Published online by Cambridge University Press

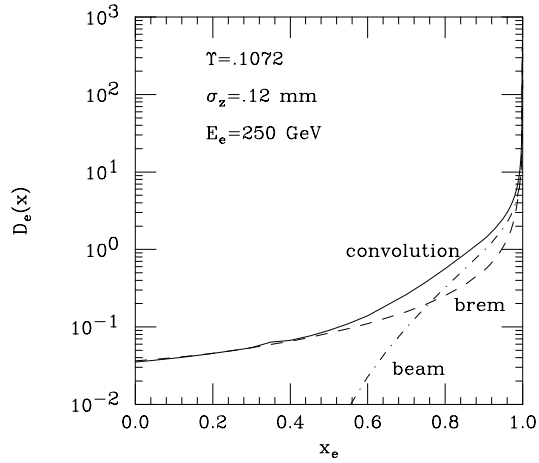


Figure 12.33 Distribution of electrons in the electron, due to bremsstrahlung, beamstrahlung and their convolution. Reprinted from H. Baer, T. Krupovnickas and X. Tata, *JHEP* **06**, 061 (2004).

parameter $\Upsilon$ along with $\sigma_z$ related to the bunch length is sufficient to determine the beamstrahlung distribution as characterized in calculations by P. Chen.[16] The beamstrahlung distribution for a collider with $\Upsilon = 0.1072$ and beam size $\sigma_z = 0.12$ mm is also shown by the dot-dashed curve in Fig. 12.33, for beam energy $E_e = 250$ GeV. To account for both bremsstrahlung and beamstrahlung, a convolution,

$$D_e(x) = \int_x^1 \mathrm{d}z D_e^{\mathrm{brem}}\left(\frac{x}{z}, Q^2\right) D_e^{\mathrm{beam}}(z)/z, \tag{12.18}$$

of the two distribution functions must be performed. The resulting beam energy distribution with both beamstrahlung and bremsstrahlung effects included is shown by the solid curve in Fig. 12.33. As can be seen, the highest probability is that electrons or positrons with $x \sim 1$ will interact. But there is a significant probability that energy loss can result from beamstrahlung and bremsstrahlung, so that the energy in the hard scattering process is considerably smaller. This is especially important when examining the reconstruction of SUSY processes with high precision, because the energy loss due to beamstrahlung/bremsstrahlung photons distorts final state distributions as well as the missing energy spectrum that is one of the key elements of sparticle production reactions.

As an example, we show the distribution in dimuon invariant mass in Fig. 12.34 for $e^+e^- \to \mu^+\mu^-$, at $\sqrt{s} = 500$ GeV, using the beamstrahlung parameters of

[16] See P. Chen, *Phys. Rev.* **D46**, 1186 (1992).

https://doi.org/10.1017/9781009289801.013 Published online by Cambridge University Press

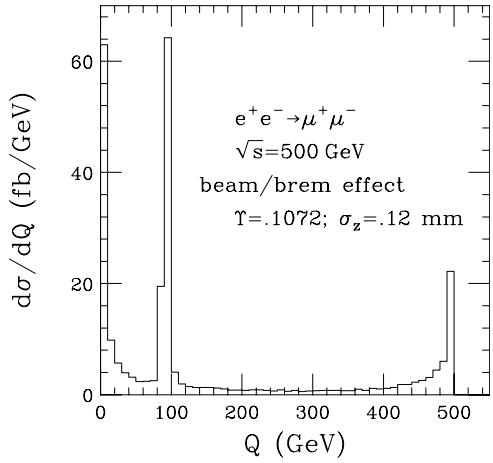


Figure 12.34 Differential cross section for muon pair production at a 500 GeV $e^+e^-$ collider, as a function of dimuon mass. The $Z$ and $\gamma$ peaks are clearly evident, due to bremsstrahlung and beamstrahlung. The two-photon background discussed in the text is not included in this figure.

Fig. 12.33. A large fraction of events is produced with invariant mass $m(\mu^+\mu^-) \sim$ 500 GeV, as might be expected. However, the $\gamma$ and $Z$ poles in the production process lead to even larger dimuon rates at $m(\mu^+\mu^-) \sim 0$ and $M_Z$.[17] In addition, there are non-vanishing cross section contributions in the intermediate invariant mass regions.

We should also mention that for very low values of $m(\mu^+\mu^-)$ the cross section will actually be dominated by the higher order process $e^+e^- \to e^+e^-\mu^+\mu^-$, where the muons are mainly produced by collision of almost on-shell photons radiated by the electron and positron beams. These "two-photon processes" are a very important background if the observable final state is a pair of charged particles with low momentum and low invariant mass and the final state electrons and positrons escape undetected down the beam pipe. Within the context of supersymmetry, this occurs when the pair-produced charged sparticle is approximately degenerate with the LSP.

[17] This means that these machines are "self-scanning" for resonances that couple to $e^+e^-$ pairs.

https://doi.org/10.1017/9781009289801.013 Published online by Cambridge University Press